DISSERTATION

submitted to the
Combined Faculty for the Natural Sciences and Mathematics
of
Heidelberg University, Germany
for the degree of
Doctor of Natural Sciences

Put forward by
M.Sc. in Physics Ecaterina Bodnariuc
Born in Chişinău, Republic of Moldova

Date of the oral examination:

On Plane Wave Ultrasound Particle Image Velocimetry

Advisor: Prof. Dr. Stefania Petra

Zusammenfassung

Diese Dissertation befaßt sich mit der Entwicklung von methodischen und mathematischen Grundlagen von *Plane Wave Ultrasound Particle Image Velocimetry* (partikelunterstützte Geschwindigkeitsmessung mittels ebene Ultraschallwellen). Diese innovative Technologie, auch bekannt als *Echo PIV*, ist eine nichtinvasive Bildgebungsmethode, die entwickelt wurde, um den Blutfluss im Gefäßsystem zu bestimmen.

In dieser Arbeit behandeln wir zwei grundlegende Probleme im Zusammenhang mit *In-Vitro*-Echo PIV. Zunächst betrachten wir das Problem der Bildrekonstruktion, welches darin besteht, die Positionen kleiner isolierter Streuer, welche in einem homogenen Medium eingebettet sind, aus Messungen mittels ebenen Ultraschallwellen (*plane waves*) abzuschätzen. Dazu verbinden wir die gängige Delay- und Sum-Methode mit der Lösung des linearen Ausgleichsproblems zum linearisierten inversen akustischen Streuungsproblem. Numerische Ergebnisse zeigen, dass das lineare Ausgleichsproblem akkurate Rekonstruktionsergebnisse liefert sowohl für synthetische als auch für *In-Vitro*-Daten.

Im zweiten Teil der Arbeit konzentrieren wir uns auf das Problem der Bewegungsschätzung für die Rohrströmung. Für laminaren und stetigen Fluss entwickeln wir einen globalen Dictionary-basierten Ansatz, der den Strömungsparameter über ein konvergierendes iteratives Verfeinerungsschema schätzt. Weiterhin zeigen wir, dass der Strömungsparameter aus der Geometrie der aus der Bildsequenz ermittelten Spektren ermittelt werden kann. Um zwischen der stationären und der turbulenten Strömung zu unterscheiden, konstruieren wir eine Filterbank, die auf alle Strömungsrichtungen reagiert und extrahieren das lokale Geschwindigkeitsfeld durch Analyse der Phasenkomponente der Antwortfunktion für kombinierte Filter. Wir validieren unsere Methoden auf synthetischen und *In-Vitro*-Daten.

Abstract

This thesis is concerned with the development of methodological and mathematical foundations of *plane wave ultrasound particle image velocimetry*. This innovative technology, also known as *Echo PIV*, is a non-invasive imaging technique developed to estimate the blood flow in the vascular system.

In this thesis, we address two relevant problems related to *in-vitro* Echo PIV. First, we consider the image reconstruction problem which amounts to estimating the location of small isolated scatterers, embedded in a homogeneous medium, from plane wave ultrasound measurements. We link the Delay and Sum method with the least-squares solution for the linearized inverse acoustic scattering problem. Numerical studies show that the least-squares approach provides accurate reconstruction results for synthetic and *in-vitro* data.

In the second part of the thesis, we focus on the motion estimation problem for pipe flow. For laminar and steady flow, we develop a global dictionary-based approach that estimates the model flow parameter via an converging iterative refinement scheme. Furthermore, we show that the flow parameter can be the determined from the geometry of the image sequence spectra. To discriminate between the steady and turbulent flow, we design a filter-bank that is sensitive to all flow directions and extract the local velocity field by analyzing the phase component of the response function for combined filters. We validate our methods on synthetic and *in-vitro* data.

Acknowledgements

I would like to thank my supervisor Prof. Stefania Petra and advisor Prof. Christoph Schnörr, both at the Faculty of Mathematics and Computer Science of Heidelberg University, for introducing me to the topic of ultrasound imaging, compressive sensing, image analysis and optimization. I am grateful for their valuable mathematical insights, criticism and support during my PhD. Many ideas presented in this thesis are the result of our joint research effort.

I would like to thank Dr. Arati Gurung, Prof. Christian Poelma from TU Delft, Netherlands, Martin F. Schiffner from Ruhr-Universität Bochum, Germany, and Jason Voorneveld from Erasmus MC Rotterdam, Netherlands, for their collaboration and many fruitful discussions about the experimental part of Echo PIV and ultrasound imaging.

I would like to thank my current and former colleagues from the *Research Training Group (RTG) 1653*, *Mathematical Imaging Group* and *Image and Pattern Analysis Group* for their wonderful company. In particular, I thank Dr. Freddie Åström, Dr. Florian Becker and Dr. Francesco Silvestri for inspiring discussions and proof-reading this thesis.

Furthermore, I would like to thank our secretaries Evelyn Wilhelm and Barbara Werner for their administrative support.

I thank my parents Sofia, Petru and my brother Gabriel for their patience, support and encouragements over the last few years.

Finally, I would like to acknowledge the financial support of the German Research Foundation (DFG) via the RTG 1653.

Contents

Chapter 1

Introduction

1.1 Motivation

Ultrasound imaging is a non-invasive technique widely used in clinical applications for diagnosis, therapeutic procedures, visualization of the internal structures and measurement of the blood flow in the body [Sza04]. Accurate assessment of the blood flow velocity field provides significant information for early detection of flow abnormalities and the diagnosis of diseases such as atherosclerosis or carotid stenosis.

Established Doppler-based methods for blood flow measurements suffer from large errors in estimating velocities due to dependencies upon the relative angle between the transmitted acoustic beam and the flow direction [Shu15]. In [KHS04], based on ideas from optical PIV in experimental fluid dynamics, a novel ultrasound velocimetry technique, so-called *Echo PIV*, has been proposed for estimating the in-plane velocity components of the blood flow. The experimental part of Echo PIV consists in seeding uniformly the blood stream with tracer particles and capturing the flow of these tracer particles by imaging a fixed region of the blood vessel for a short period. It is assumed that for this period the tracer particles follow the flow dynamics and move within the imaging plane. The in-plane velocity field of the flow is then estimated from the acquired sequence of ultrasound images. In contrast to Doppler-based methods, Echo PIV is independent of the beam transmission angle and can provide an accurate velocity field estimate. Specifically, accurate measurements of the velocity field near the vessel wall is needed for computing the wall shear stress and the blood vessel stiffness [PvdMM+12]. These parameters are important for the diagnosis of atherosclerosis. Moreover, Echo PIV is an excellent tool to study vortex dynamics in ventricles [HPT+08]. For an extensive review on Echo PIV we refer to [Poe17] and references therein.

Recent technological developments have made it possible to image wide field of views at very high frame rates by simultaneously transmitting and receiving with all ultrasound transducer elements [SCT+99, TBSF02, TF14]. This image acquisition scheme is called *plane wave ultrasound imaging*. Hence, the *plane wave ultrasound*

particle image velocimetry, or plane wave Echo PIV, is capable to resolve fast and dynamic flow due to an enhanced temporal resolution of the image sequence. The plane wave imaging was implemented in *in-vitro* Echo PIV [RJG13, LBE+15] and further extended to 3D imaging in the works [PPA+14, CPTP16].

Mathematical challenges related to ultrasound-based imaging primarily consists in interpreting and extracting relevant information from the received ultrasound signals. In particular, the research on plane wave Echo PIV is concerned with the problems of (i) image reconstruction and (ii) motion estimation.

Image reconstruction can be formulated as an inverse acoustic scattering problem for the wave equation. The literature on this subject is vast, here, we mention the books [CCM00, BCS01, AGJ+13] for theoretical insights. Various reconstruction approaches have been adopted from geophysicists and generalized to plane wave ultrasound imaging such as Delay and Sum [MTB+09], topological imaging [RSGJ12, DG10] and Stolt's f-k migration [GTM+13]. Recently, reconstruction with sparsity promoting priors in the context of compressive sensing [FR13] has received much attention from practitioners [SS12, CE14, DRZL15, BZV+16]. Resolution analysis and recovery guarantees have been presented in [CMP13, CMP14, Bor15] for asymptotic scenarios and point-like scatterers. Those studies for narrow- and broad-band imaging are based on mutual coherence of the sensing matrix in frequency domain. From a practical point of view, however, the sensing matrix in the frequency domain does not scale well for the large problem sizes encountered in ultrasound imaging problems, due to memory requirements for non-sparse sampling operators.

The problem of motion estimation in image sequences occur in many application areas. In particular, in Echo PIV motion estimation amounts to determining the components of the in-plane velocities that describe the flow of tracer particles from one image to another. As in optical PIV, the velocity field is commonly estimated by using cross-correlation based methods [RWWK07, Adr11].

1.2 Contribution

This thesis studies the problem of image reconstruction and motion estimation related to plane wave *in-vitro* Echo PIV, illustrated in Figure 1.1. The contributions are:

- First, we propose a mathematical model based on acoustic scattering theory to recover the location of isolated scatterers from plane wave ultrasound measurements. Relying on specific assumptions, we derive a linear relationship between the measured data and the unknown medium reflectivity. We solve numerically the discrete sparse linear system using least-squares minimization with various regularization terms. We experimentally validate the proposed approach on realistic large scale problems, see Chapter 3.

- Second, we propose to estimate the motion by computing the flow model parameter defining the velocity profile in pipe flow, see Section 2.2.3. For laminar and steady flow we propose a global dictionary-based approach which amounts to defining a twice continuously differentiable map with respect to the flow parameter, and estimate the flow model parameter by minimizing an appropriate objective function, see Chapter 4. In addition, we analyze properties of the image sequence spectrum for affine flows and show that the flow model parameter can be estimated from the spectrum geometry, see Section 5.1. In Section 5.3, we propose a filter-based method to compute the local flow velocity field.

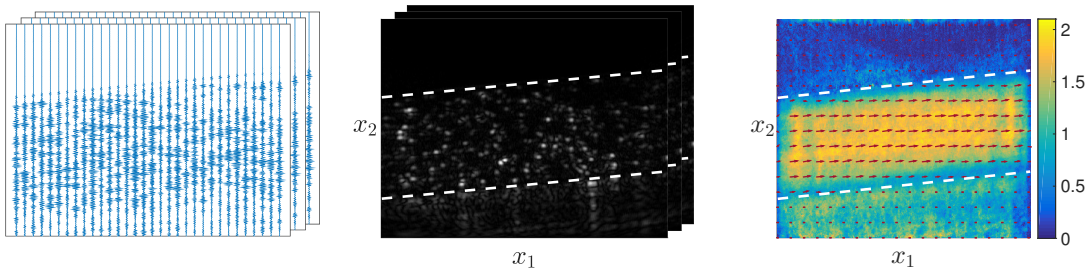

(a) (b) (c)

Figure 1.1: (a) The ultrasound measurements of the backscattered waves recorded at several temporal frames. (b) Reconstructed images of tracer particles with the approach presented in Chapter 3. (c) Velocity field estimated with the local spatio-temporal approach presented in Section 5.3. The image reconstruction step (a) $\rightarrow$ (b) and motion estimation step (b) $\rightarrow$ (c) are the main topics treated in this thesis.

Parts of this thesis are included in the following publications:

[BGPS15] E. Bodnariuc, A. Gurung, S. Petra, and C. Schnörr. Adaptive Dictionary-Based Spatio-temporal Flow Estimation for Echo PIV. In *Proc. EMMCVPR*, volume 8932 of *LNCS*, pages 378–391. Springer, 2015

[BPPS16] E. Bodnariuc, S. Petra, C. Poelma, and C. Schnörr. Parametric Dictionary-Based Velocimetry for Echo PIV. In *GCPR*, volume 9796 of *Lecture Notes in Computer Science*, pages 332–343. Springer, 2016

[BSPS16] E. Bodnariuc, M. Schiffner, S. Petra, and C. Schnörr. Plane Wave Acoustic Superposition for Fast Ultrasound Imaging. In *International Ultrasonics Symposium (IUS)*. IEEE, 2016

[BPSV17] E. Bodnariuc, S. Petra, C. Schnörr, and J. Voorneveld. A Local Spatio-Temporal Approach to Plane Wave Ultrasound Particle Image Velocimetry. In *GCPR*, volume 10496 of *Lecture Notes in Computer Science*, pages 138–149, 2017

[Bod18] E. Bodnariuc. A Spectral Approach to Peak Velocity Estimation of Pipe Flows from Noisy Image Sequences. *Analele Stiintifice ale Univesitatii Ovidius Constanta*, 2018. (accepted)

The image reconstruction approach presented in Chapter 3 is based on [BSPS16]. Chapter 4 extends the dictionary-based method for flow parameter estimation introduced in [BGPS15, BPPS16]. The material in Chapter 5 collects the results of [Bod18, BPSV17].

Chapter 2

Background

In this chapter we present the basics of acoustic scattering theory and plane wave ultrasound particle image velocimetry. We introduce the forward scattering problem in temporal and frequency domain, the Born approximation, and review the Foldy-Lax method for solving the forward acoustic scattering problem for point-like scatterers. For a detailed treatment of these topics we refer to [CK13, BCS01, Pie89]. The second part of the chapter is dedicated to practical aspects of plane wave ultrasound imaging and *in-vitro* Echo PIV.

2.1 Acoustic Scattering Theory

2.1.1 Wave Equation

Propagation of acoustic waves in linear, lossless and static medium is described by the scalar wave equation

$$\left(\nabla^2 - \frac{1}{c^2(x)}\frac{\partial^2}{\partial t^2}\right) u(x,t) = 0, \quad x \in \mathbb{R}^3, t > 0, \tag{2.1.1}$$

where $c(x)$ denotes the local speed of sound and $u(x,t)$ is the pressure field of the acoustic wave. The *radiating* solution of the wave equation satisfies the *Sommerfeld radiation condition*

$$\lim_{r\to\infty}\left[r\left(\frac{\partial u}{\partial r} + \frac{1}{c}\frac{\partial u}{\partial t}\right)\right] = 0, \quad r = \|x\|_2, \tag{2.1.2}$$

uniformly in all directions $x/\|x\|_2$. We further assume that medium inhomogeneities are contained inside a compact subset $\Omega \in \mathbb{R}^3$ and that the speed of sound $c(x)$ is a perturbation of the constant background speed of sound $c_0 > 0$, namely

$$\frac{1}{c^2(x)} = \frac{1}{c_0^2}\left(1 - \rho(x)\right), \tag{2.1.3}$$

where $\rho(x)$ denotes the *reflectivity* due to the medium inhomogeneities. Hence, we have $\rho(x) = 0$ for $x \notin \Omega$. Substituting (2.1.3) into (2.1.1) yields the non-homogeneous wave equation

$$\left(\nabla^2 - \frac{1}{c_0^2}\frac{\partial^2}{\partial t^2}\right) u(x,t) = f(x,t), \quad x \in \mathbb{R}^3, t > 0, \tag{2.1.4}$$

with

$$f(x,t) = -\frac{\rho(x)}{c_0^2}\frac{\partial^2 u(x,t)}{\partial t^2}. \tag{2.1.5}$$

In acoustic scattering problems, when a known incident field interacts with inhomogeneities and produces a scattered field, it is convenient to split the total field, the pressure field, into two parts as follows

$$u(x,t) = u^{(i)}(x,t) + u^{(s)}(x,t). \tag{2.1.6}$$

The first term, $u^{(i)}(x,t)$, denotes the *incident field* and satisfies the homogeneous wave equation

$$\left(\nabla^2 - \frac{1}{c_0^2}\frac{\partial^2}{\partial t^2}\right) u^{(i)}(x,t) = 0, \quad x \in \mathbb{R}^3, t > 0. \tag{2.1.7}$$

The second term, $u^{(s)}(x,t)$, is the *scattered field* resulting from the interaction of the incident field with the medium inhomogeneities or scatterers, which in view of (2.1.4)-(2.1.7) must satisfy

$$\left(\nabla^2 - \frac{1}{c_0^2}\frac{\partial^2}{\partial t^2}\right) u^{(s)}(x,t) = f(x,t), \quad x \in \mathbb{R}^3, t > 0, \tag{2.1.8}$$

and the Sommerfeld radiation condition (2.1.2). In the following analysis, we restrict the time domain to $t > 0$ due to the *causality* condition, meaning that the interaction of the incident field with the inhomogeneities (scatterers) is initiated at some finite time that we take to be $t = 0$. Furthermore, we can impose the initial conditions

$$u^{(s)}(x,0) = 0, \quad \frac{\partial u^{(s)}(x,0)}{\partial t} = 0, \quad x \in \mathbb{R}^3, \tag{2.1.9}$$

and use Duhamel's principle [Eva10] to express the scattered field in terms of an integral equation

$$u^{(s)}(x,t) = \int_0^t \int_{\mathbb{R}^3} f(y,s)G(x-y,t-s)\mathrm{d}y\mathrm{d}s, \tag{2.1.10}$$

where $G(x-y,t-s)$ is the causal Green's function satisfying

$$\left(\nabla_x^2 - \frac{1}{c_0^2}\frac{\partial^2}{\partial t^2}\right) G(x-y,t) = \delta(x-y)\delta(t), \quad x, y \in \mathbb{R}^3,\ t > 0, \tag{2.1.11}$$

$$G(x-y,t) = 0, \qquad t < 0, \tag{2.1.12}$$

in the sense of distributions. Physically speaking, the function $G(x-y,t)$ represents the acoustic pressure at the point $x \neq y$ and $t > 0$, caused by a source located at point y and time $t = 0$. Because the Green's function and $f(x,t)$ are assumed to be causal[1], we rewrite (2.1.10) as

$$u^{(s)}(x,t) = \int_{\mathbb{R}^3} f(y,t) \star_t G(x-y,t) \mathrm{d}y \tag{2.1.13a}$$

$$\overset{(2.1.5)-(2.1.6)}{=} -\frac{1}{c_0^2} \int_{\mathbb{R}^3} \rho(y) \frac{\partial^2}{\partial t^2} (u^{(i)}(y,t) + u^{(s)}(y,t)) \star_t G(x-y,t) \mathrm{d}y, \tag{2.1.13b}$$

where $\star_t$ denotes the convolution operator.

2.1.2 Forward Scattering Problem

The *forward scattering problem* is to find the scattered wave given the incident wave and the reflectivity of the medium, that is, to solve the non-linear equation (2.1.13) for $u^{(s)}(x,t)$. It is convenient to reformulate the scattering problem in the frequency (Fourier) domain. We will use the following forward and inverse *temporal* Fourier transform convention

$$(\mathcal{F}u)(x,\omega) = \hat{u}(x,\omega) = \int u(x,t) e^{+i\omega t} \mathrm{d}t, \tag{2.1.14}$$

$$(\mathcal{F}^{-1}\hat{u})(x,t) = u(x,t) = \frac{1}{2\pi} \int \hat{u}(x,\omega) e^{-i\omega t} \mathrm{d}\omega. \tag{2.1.15}$$

From now on, we assume that the known incident field $\hat{u}^{(i)}(x,\omega)$ is a smooth function supported at $\omega > 0$. In the frequency domain, equation (2.1.1), (2.1.6), (2.1.7) and (2.1.8) form the system of equations

$$\left(\nabla^2 + \frac{\omega^2}{c_0^2}(1-\rho(x))\right) \hat{u}(x,\omega) = 0, \tag{2.1.16}$$

$$\hat{u}(x,\omega) = \hat{u}^{(i)}(x,\omega) + \hat{u}^{(s)}(x,\omega), \tag{2.1.17}$$

$$\left(\nabla^2 + \frac{\omega^2}{c_0^2}\right) \hat{u}^{(i)}(x,\omega) = 0, \tag{2.1.18}$$

$$\left(\nabla^2 + \frac{\omega^2}{c_0^2}\right) \hat{u}^{(s)}(x,\omega) = \frac{\omega^2}{c_0^2} \rho(x) \hat{u}(x,\omega), \tag{2.1.19}$$

for $x \in \mathbb{R}^3$ and $\omega > 0$. For the outgoing scattered wave, the system is complemented by the Sommerfeld radiation condition

$$\lim_{r\to\infty} \left[r \left(\frac{\partial \hat{u}^{(s)}}{\partial r} - ik\hat{u}^{(s)} \right) \right] = 0, \quad r = \|x\|_2. \tag{2.1.20}$$

[1] Causality condition assumes that $G(x-y,t) = f(x,t) = 0$ for $t < 0$.

uniformly in all directions $x/\|x\|_2$. The angular frequency ω is related to the *wave number* k and the wave speed c_0 via $k = \omega/c_0$. It is measured in radians per seconds and differs by a factor 2π from the frequency (measured in Hz).

The scattering problem for an inhomogeneous medium (2.1.16) - (2.1.20) is equivalent to an integral equation, known as the *Lippmann-Schwinger* equation

$$\hat{u}(x,\omega) = \hat{u}^{(i)}(x,\omega) + \frac{\omega^2}{c_0^2}\int_{\mathbb{R}^3} \rho(y)\hat{u}(y,\omega)g(x-y,\omega)\mathrm{d}y \tag{2.1.21}$$

where $g(x-y,\omega)$ is known as the *fundamental solution*, or the free space Green's function of the Helmholtz equation

$$\left(\nabla_x^2 + \frac{\omega^2}{c_0^2}\right) g(x-y,\omega) = 0, \quad x \in \mathbb{R}^3 \setminus \{y\} \tag{2.1.22}$$

satisfying the radiation condition (2.1.20), given by

$$g(x-y,\omega) := \frac{1}{4\pi}\frac{e^{i\omega\|x-y\|/c_0}}{\|x-y\|}, \quad x \neq y. \tag{2.1.23}$$

From (2.1.21) we see that

$$\hat{u}^{(s)}(x,\omega) = \frac{\omega^2}{c_0^2}\int_{\mathbb{R}^3} \rho(y)\hat{u}(y,\omega)g(x-y,\omega)\mathrm{d}y \tag{2.1.24a}$$

$$= \frac{\omega^2}{c_0^2}\int_{\mathbb{R}^3} \rho(y)(\hat{u}^{(i)}(y,\omega) + \hat{u}^{(s)}(y,\omega))g(x-y,\omega)\mathrm{d}y. \tag{2.1.24b}$$

In the frequency domain the scattered field still fulfills a non-linear integral equation, however, the advantage of working in the frequency domain is that the second derivative with respect to time in (2.1.13) is substituted by the term $-\omega^2$ and the convolution becomes a product. We refer to [CK13, Kir11, Kre10] for an extended discussion on the uniqueness and existence of the solution for the Lippman-Schwinger integral equation (2.1.21), which is a Fredholm integral equation of the second kind.

2.1.3 Born Approximation

We notice that for $\rho(y) \equiv 0$ the scattered field in (2.1.24) vanishes. Therefore, it is reasonable to assume that when the reflectivity ρ is small, the scattered field is also small, in particular $\rho(y)\hat{u}^{(s)}(y,\omega) \ll \rho(y)\hat{u}^{(i)}(y,\omega)$. The Born approximation replaces the total field on the right hand side of (2.1.24) with the known incident field, resulting in

$$\hat{u}^{(s)}(x,\omega) \approx \frac{\omega^2}{c_0^2}\int_{\mathbb{R}^3} \rho(y)\hat{u}^{(i)}(y,\omega)g(x-y,\omega)\mathrm{d}y. \tag{2.1.25}$$

The above scattered field is accurate up to the first order in reflectivity $\rho(y)$. The Born approximation turns the forward and inverse scattering problem into a linear problem and therefore is often employed in practical applications. It is also known as the *weak-scattering* or *single-scattering* approximation as it ignores multiple scattering effects. We refer to [Nat15] for an error estimation of this approximation.

2.1.4 Foldy-Lax Equation

The multiple scattering effects, neglected in the Born approximation, can be modeled via the Foldy-Lax equation [Fol45, Lax51] that is valid for isotropic point-like scatterers. We consider the scattering of monochromatic incident waves by $S \in \mathbb{N} \setminus \{0\}$ point-like scatterers located at y_j, $j \in [S]$, in a homogeneous medium. The Foldy-Lax equation states that the total field at the location of the scatterer j is given by

$$u(y_j) = u^{(i)}(y_j) + \sum_{j'=[S], j' \neq j} \rho_{j'} u(y_{j'}) g(y_j - y_{j'}, \omega), \tag{2.1.26}$$

where $\rho_{j'} \in \mathbb{R} \setminus \{0\}$ is the reflectivity of the j' scatterer, $g(y_j - y_{j'}, \omega)$ is the Green's function defined in (2.1.23), $u(y_j)$ denotes the spatial component of the monochromatic total field $\hat{u}(y_j, \omega) = u(y_j) e^{i\omega t}$ and $u^{(i)}(y_j)$ denotes the spatial component of incident field $\hat{u}^{(i)}(y_j, \omega) = u^{(i)}(y_j) e^{i\omega t}$. The above equation defines the total field as the sum of the incident wave and spherical waves diverging from all scatterers except from scatterer j. The total field at a different point in space $y \neq y_j$, $j \in [S]$ is given by

$$u(y) = u^{(i)}(y) + \sum_{j=[S]} \rho_j u(y_j) g(y - y_j, \omega). \tag{2.1.27}$$

The system of linear equations in (2.1.26) can be written in matrix form

$$b = Mu, \tag{2.1.28}$$

where M is the Foldy-Lax matrix with entries

$$M_{ij} = \begin{cases} 1, & \text{if } i = j, \\ -\rho_j g(y_i - y_j, \omega), & \text{if } i \neq j, \end{cases} \tag{2.1.29}$$

and

$$b = (u^{(i)}(y_1)\ u^{(i)}(y_2)\ \ldots\ u^{(i)}(y_S))^T \in \mathbb{R}^S,$$

$$u = (u(y_1)\ u(y_2)\ \ldots\ u(y_S))^T \in \mathbb{R}^S,$$

are vectors whose components are the incident and total fields at the location of S scatterers. Matrix M is a perturbation of the $S \times S$ identity matrix, which becomes diagonal dominant and hence invertible for a sufficiently large separation distance between scatterers or for small reflectivity ρ_j, $j \in [S]$.

Lemma 2.1.1. *Matrix M defined in (2.1.29) can be decomposed as $M = I - A$. If the matrix norm*

$$\|A\|_\infty = \max_i \sum_{j\in[S], j\neq i} \frac{|\rho_i|}{4\pi\|y_i - y_j\|} < 1,$$

(in particular, when ρ_i is sufficiently small or $\|y_i - y_j\|$ is sufficiently large) then M is invertible and

$$M^{-1} = (I - A)^{-1} = 1 + A^1 + A^2 + \dots \tag{2.1.30}$$

Proof. The assertion follows immediately from [Wer11, Theorem II.1.11]. □

Solving (2.1.28) for vector u and substituting the corresponding entries $u(y_j)$, $j \in [S]$, in equation (2.1.27) we obtain the total field as a function of position and reflectivity, that accounts for multiple scattering. In the case of very weak scatterers, the total field in (2.1.26) can be approximated by the incident field $u(y_j) \approx u^{(i)}(y_i)$ in (2.1.27), resulting in

$$u(y) = u^{(i)}(y) + \sum_{j=[S]} \rho_j u^{(i)}(y_j) g(y - y_j, \omega), \tag{2.1.31}$$

for $y \neq y_j$, $\forall j \in [S]$, which is the total field under the Born approximation.

2.1.5 Inverse Scattering Problem

The *inverse scattering problem* is to determine the reflectivity $\rho(x)$ from the observed data, i.e. the scattered field, and the known incident field. The non-linear equation (2.1.24) relates the reflectivity $\rho(y)$ and the scattered field, which can not be solved in general for incomplete observation data. The simplest strategy is to linearize the problem using Born approximation. The resulting equation (2.1.25) is a Fredholm integral equation of the first kind, which usually is unstable and hence *ill-posed*, i.e. a small change in the data term $u^{(s)}$ may lead to an arbitrarily large change in the solution for reflectivity ρ. The definition given by Hadamard [Had23] states that a problems is *well-posed* if it satisfies three requirements: a solution exist, the solution is unique, and the solution depends continuously on the data. Otherwise, the problem is *ill-posed*.

In this thesis, we consider a simpler version of the inverse scattering problem. We seek an approximative location of the inhomogeneous structures by further simplifying (2.1.25) and thus making simplifying assumptions on the waves propagate through the medium.

2.2 Ultrasound Particle Image Velocimetry

Ultrasound imaging, widely used in medical applications, provides a non-invasive imaging modality to visualize internal body structures. In ultrasound imaging, a region of interest is probed by acoustic waves emitted by an array of transducer elements, i.e.

sources of acoustic waves. With the measured backscattered waves picked up at the receivers, which are the same transducer elements, one can reconstruct a two dimensional gray scale image of the medium.

In this thesis, we focus on a particular type of ultrasound imaging technique, namely *plane wave ultrasound particle image velocimetry* (also known as *Echo PIV*), that was developed to assess blood flow velocity field and the wall shear stress in blood vessels [KHS04, PvdMM+12]. The main idea of Echo PIV is to seed the blood flow with tracer particles and capture a temporal image sequence of these moving particles. In a post-processing step, the in-plane velocity field components of the flow can then be estimated.

2.2.1 Ultrasound Imaging

Line-per-line imaging with focused acoustic beams is currently implemented in almost all medical ultrasound machines, where an image of a wide field of view is created sequentially. This works as follows. A small subset of transducer elements (or only one element) emit a focused beam which probes a narrow segment in the medium, as illustrated in Figure 2.1 (a). Then the same subset of elements receive the backscattered signal and after a fairly simple signal processing step, that assumes straight line propagation of the sound, a column in the image is reconstructed. Next column is obtained by probing the medium in the same way with the following subset of elements and so-forth, until the entire field of view is scanned. For motion estimation tasks, line-per-line imaging is rather slow, limiting the resolvable range of velocities and inducing beam sweeping effects [PvdMM+12].

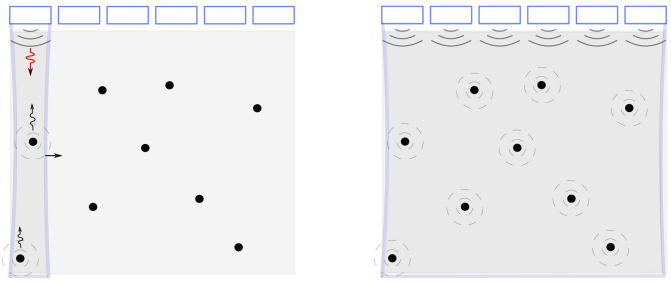

(a) (b)

Figure 2.1: Illustration of source-receiver configurations. (a) Sequential line-per-line imaging. (b) Plane wave imaging.

Recent hardware and software developments made it possible for an ultrasound transducer to simultaneously transmit and receive with all elements. By emitting an acoustic pulse with all elements of a linear array, a quasi-planar wavefront of an acoustic pulse is generated and transmitted into the medium, probing simultaneously a wide field of view, as shown in Figure 2.1 (b). From the measurements of the backscattered

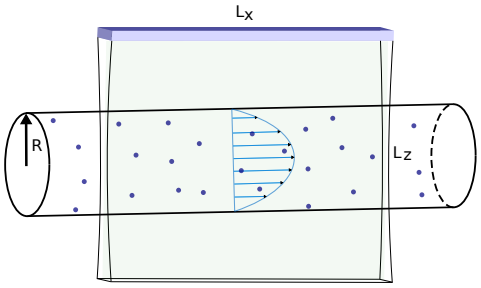

Figure 2.2: Schematic overview of the *in vitro* Echo PIV experiment. A linear transducer array aligned along the tube axis probes a thin slice at the center of the tube by transmitting and receiving acoustic waves. The received data are radio frequency signals. After a reconstruction step, a gray scale image of the tracer particles is obtained.

waves at the location of the transducer elements, an image of the medium can be reconstructed. We refer to this source-receiver configuration as *plane wave ultrasound imaging*.

In contrast to sequential line-per-line acquisition, the imaging frame rate with plane waves transmission is limited only by the speed of acoustic waves inside the probed medium and the relaxation time between receiving and transmitting modes of the ultrasound transducer [CFT12]. With a frame rate of thousands of images per seconds (kHz range), plane wave ultrasound imaging provides an excellent tool for measuring complex and dynamic flows such as cardiac and vascular blood flow.

2.2.2 *In Vitro* EchoPIV

In this thesis we restrict our attention to the *in-vitro* Echo PIV experiment, which is designed as follows. A fluid imitating blood is seeded with tracer particles, i.e. gas-bubbles, and pumped through a straight horizontal cylindrical tube that mimics a blood vessel. The flow of the fluid is set to a specific, constant flow rate. The flow of tracer particles is imaged at the central plane of the tube by aligning the ultrasound linear transducer array along the tube axis, as illustrated in Figure 2.2. With plane wave image acquisition scheme, the moving fluid is probed at a very high frame rate. After the image reconstruction step, the image sequence capturing the tracer particles flow is analysed and the in-plane velocity field at the central plane of the tube is estimated.

2.2.3 Laminar Pipe Flow

If the pipe flow in *in-vitro* Echo PIV is *laminar and steady*, also known as Poiseuille flow, then in-plane velocity field is given by

$$u = u(x) = \Big(u_1(x_2), 0\Big)^\top, \qquad u_1(x_2) = v_m\Big(1 - \Big(\frac{x_2}{R}\Big)^2\Big), \qquad v_m \geq 0, \tag{2.2.1}$$

where v_m denotes the peak velocity of the flow in a pipe of radius R, assumed to be centered at $x_2 = 0$. Thus, the flow has a parabolic profile, does not depend on x_1, and hence has a single degree of freedom v_m.

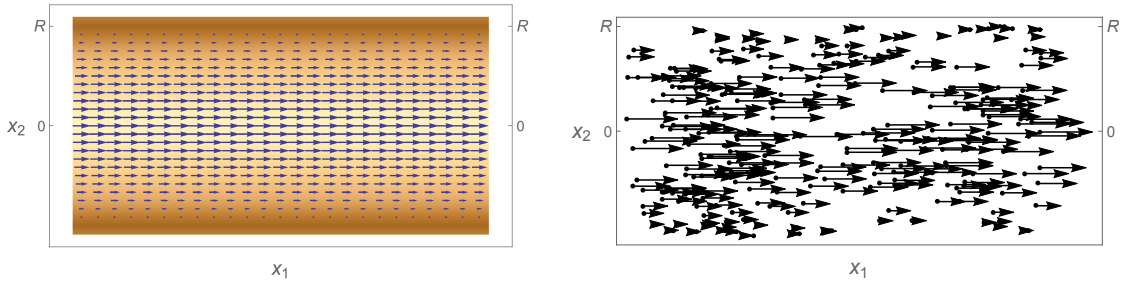

Figure 2.3: LEFT: A Poiseuille flow governed by (2.2.1). The background illustrates the parabolic velocity profile parametrized by the pipe radius R and the peak velocity v_m. RIGHT: An *unknown* set of randomly located particles that are moving with the flow. The task is to robustly estimate the *unknown* peak velocity v_m and consequently the velocity field under adverse imaging conditions from noisy image sequence data.

This smooth and laminar flow occurs at moderate Reynolds numbers. At larger Reynolds numbers the flow becomes *turbulent* and exhibits motion instability. Such flows are unsteady and irregular, yet appear steady and predictable after temporal averaging of the velocity field [Whi09]. There are many empirical formulas describing the velocity profile of turbulent flow in a pipe. Here, we adopt the representation proposed in [Sti14] in terms of the velocity field

$$u = u(x) = \Big(u_1(x_2), 0\Big)^\top, \quad u_1(x_2) = v_m\bigg(1 - \Big(\frac{|x_2|}{R}\Big)^{N+1}\bigg). \tag{2.2.2}$$

With this representation, for $N = 1$ we recover the parabolic velocity profile of (2.2.1) and for $N > 1$ a deformed velocity profile is obtained.

Chapter 3

Ultrasound Image Reconstruction

In this chapter we formulate ultrasound imaging as an inverse acoustic scattering problem for the wave equation, where for a given incident plane wave pulse, the problem is to estimate the location of medium inhomogeneities (i.e. the tracer particles) from the backscattered waves received by the ultrasound transducer array. Based on a set of specific assumptions, we derive a simplified relationship between the measured data and the unknown medium reflectivity. We discretize the problem by using the collocation method and solve the corresponding algebraic system of linear equations by least-squares minimization. The approach is validate on synthetic and *in-vitro* Echo PIV data.

3.1 Imaging Operator

3.1.1 The Model Problem

Under the Born approximation, presented in Section 2.1.3, the reflectivity and the scattered field are related by the linear integral equation

$$\hat{u}^{(s)}(x,\omega) = \frac{\omega^2}{c_0^2} \int_{\mathbb{R}^3} \rho(y)\hat{u}^{(i)}(y,\omega)g(x-y,\omega)\mathrm{d}y. \tag{3.1.1}$$

In the ultrasound imaging context, the function $\hat{u}^{(s)}(x,\omega)$ represents measured data at a finete set of points in time domain and the function ρ contains information about the location of the acoustic scatteres that has to be determined. Furthermore, the incident field and the Green functions is known. In particular, the transmitted incident field is a plane wave pulse focused in one direction probing only a thin slice of the medium as can be seen in Figure 2.2. Therefore, we assume the incident field to be given by

$$\hat{u}^{(i)}(y,\omega) = f(\omega)e^{i\omega\langle d,y\rangle/c_0}\chi_{[-\varepsilon_3/2,\varepsilon_3/2]}(y_3), \quad y = (y_1,y_3,y_3), \tag{3.1.2}$$

where χ is a characteristic function, $\varepsilon_3 > 0$ is the width of the probed slice, $f(\omega)$ denotes the frequency-dependent amplitude of the incident wave defining the shape

of the pulse (for example a Gaussian pulse), and $d \in S^2$ specifies the direction of incidence. Substituting (2.1.23) and (3.1.2) into (3.1.1), yields

$$\hat{u}^{(s)}(x,\omega) = \frac{\omega^2 f(\omega)}{4\pi c_0^2} \int_{\mathbb{R}^3} \rho(y) \frac{e^{i\omega(\langle d,y\rangle + \|x-y\|)/c_0}}{\|x-y\|} \chi_{[-\varepsilon_3/2,\varepsilon_3/2]}(y_3) \mathrm{d}y. \tag{3.1.3}$$

By applying the inverse Fourier transform (2.1.15) we obtain the scattered field in time domain

$$u^{(s)}(x,t) = \frac{1}{2\pi} \int_{\mathbb{R}} \hat{u}^{(s)}(x,\omega) e^{-i\omega t} \mathrm{d}\omega \tag{3.1.4a}$$

$$= \frac{1}{8\pi^2 c_0^2} \int_{\mathbb{R}} \mathrm{d}\omega \int_{\mathbb{R}^3} \omega^2 f(\omega)\rho(y) \frac{e^{i\omega(\langle d,y\rangle + \|x-y\|)/c_0}}{\|x-y\|} e^{-i\omega t} \chi_{[-\varepsilon_3/2,\varepsilon_3/2]}(y_3) \mathrm{d}y. \tag{3.1.4b}$$

According to [Bor15], the term $\omega^2 f(\omega)$ can be safely ignored if the incident pulse is very short in time. Equation (3.1.4b) can be further simplified by ignoring the term $\frac{1}{\|x-y\|}$. Hence, the measured data $d(x,t) \propto u^{(s)}(x,t)$ can be expressed as

$$d(x,t) \propto \int_{\mathbb{R}} \mathrm{d}\omega \int_{\mathbb{R}^3} \rho(y) e^{i\omega(\langle d,y\rangle + \|x-y\|)/c_0 - i\omega t} \chi_{[-\varepsilon_3/2,\varepsilon_3/2]}(y_3) \mathrm{d}y \tag{3.1.5a}$$

$$\propto \int_{\mathbb{R}^2} \rho(y) \delta\left(\frac{\langle d,y\rangle}{c_0} + \frac{\|x-y\|}{c_0} - t \right) \Big|_{y_3=0} \mathrm{d}y_1 \mathrm{d}y_2. \tag{3.1.5b}$$

Next, we remove the redundant dimension in y_3 direction, and regard the reconstruction problem as two dimensional. We denote the image domain by

$$\Omega = (0,l_1) \times (0,l_2) \in \mathbb{R}^2, \quad l_1, l_2 > 0,$$

as illustrated in Figure 3.1, and set the location of receivers array at

$$x = (x_1, x_2) \in (0,l_1) \times \{0\}.$$

We consider the incident wave to be transmitted in the direction $d = (0,1)$ and the backscattered waves to be measured at the time $t \in [0,T], T > 0$, with $T = 2l_2/c_0$. Furthermore, we define the forward map $\mathcal{K} : L^2(\Omega) \to L^2((0,l_1) \times [0,T])$ as a linear integral operator

$$[\mathcal{K}\rho](x_1,t) := d(x_1,t) \tag{3.1.6a}$$

$$= \int_{\Omega} \rho(y_1,y_2) \delta\left(\frac{y_2 + \sqrt{(x_1-y_1)^2 + y_2^2}}{c_0} - t \right) \mathrm{d}y_1 \mathrm{d}y_2, \tag{3.1.6b}$$

that takes the reflectivity function and maps it to the measurements. The reflectivity function describes the medium inhomogeneities, which in our application is represented by the tracer particles. We may assume that those tracer particles are smooth

objects with compact support so that $\rho \in \mathbb{C}_0^\infty(\Omega)$ and both (3.1.6a) and (3.1.6b) are well defined.

An estimate of the unknown reflectivity can be obtained by minimizing the data misfit

$$O(\rho) = \|d - \mathcal{K}\rho\|^2_{L^2((0,l_1)\times[0,T])} \tag{3.1.7a}$$

$$= \int_{t\in[0,T]} \int_{x_1\in(0,l_1)} \|d(x_1,t) - [\mathcal{K}\rho](x_1,t)\|^2 \mathrm{d}t\mathrm{d}x_1. \tag{3.1.7b}$$

The minimizer of (3.1.7) satisfies the normal equation

$$[\mathcal{K}^*\mathcal{K}\rho](y) = [\mathcal{K}^* d](y), \quad \forall y \in \Omega, \tag{3.1.8}$$

where the operator $\mathcal{K}^* : L^2((0,l_1)\times[0,T]) \to L^2(\Omega)$ is the adjoint of $\mathcal{K}$, defined by the relation

$$\langle d, \mathcal{K}\rho\rangle_{L^2((0,l_1)\times[0,T])} = \langle \mathcal{K}^* d, \rho\rangle_{L^2(\Omega)}, \tag{3.1.9}$$

for all $d \in L^2((0,l_1)\times[0,T])$ and all $\rho \in L_2(\Omega)$. The symmetric operator $\mathcal{K}^*\mathcal{K} : L^2(\Omega) \to L^2(\Omega)$ is called the *normal operator*.

3.1.2 Delay and Sum (DAS)

In *Kirchhoff migration imaging*, the normal operator $\mathcal{K}^*\mathcal{K}$ is approximated by the identity operator [Bor15, CMP13]. Thus, according to (3.1.8), the reflectivity can be evaluated by applying the adjoint operator $\mathcal{K}^*$ directly to the data, that is

$$\rho(y) \approx [\mathcal{K}^* d](y) \tag{3.1.10a}$$

$$= \int_{t\in[0,T]} \int_{x_1\in(0,l_1)} d(x_1,t)\delta\left(\frac{y_2 + \sqrt{(x_1-y_1)^2 + y_2^2}}{c_0} - t\right) \mathrm{d}t\mathrm{d}x_1. \tag{3.1.10b}$$

Equation (3.1.10) provides an approximative solution of the least squares problem in (3.1.7). In the applied literature on plane wave ultrasound imaging, image formation via (3.1.10) is known as *Delay and Sum* (DAS) method [SCT+99, MTB+09, BGPT01]. The DAS approach can be physically interpreted as follows. The measured data $d(x_1,t)$ are backprojected to the two-way travel time

$$t = \tau_1(y) + \tau_2(x,y) = \frac{y_2}{c_0} + \frac{\sqrt{(x_1-y_1)^2 + y_2^2}}{c_0}$$

by the delta distribution, and summed up coherently over all receivers to obtain an estimate of the reflectivity $\rho(y)$ at any point $y = (y_1, y_2) \in \Omega$. The stability of the Kirchhoff migration imaging with respect to the measurement noise is investigated in [AGK+11, AGJ+13].

3.1.3 Discretization by Collocation Method

For numerical treatment, we discretize the continuous problem (3.1.6) using the collocation method [Kir11] and reduce it to a finite system of linear equations. We discretize the image domain Ω into an $N = n_1 \times n_2$ array of *pixels* and approximate the reflectivity by series expansion as follows

$$\rho(y_1, y_2) = \sum_{j \in [N]} \rho_j \psi_j(y_1, y_2), \tag{3.1.11}$$

where the orthogonal basis functions $\{\psi_j\}_{j \in [N]}$ are induced by the discretization of Ω and chosen as

$$\psi_j(y_1, y_2) = \begin{cases} 1, & \text{if } (y_1, y_2) \text{ is inside the } j\text{th pixel,} \\ 0, & \text{otherwise.} \end{cases} \tag{3.1.12}$$

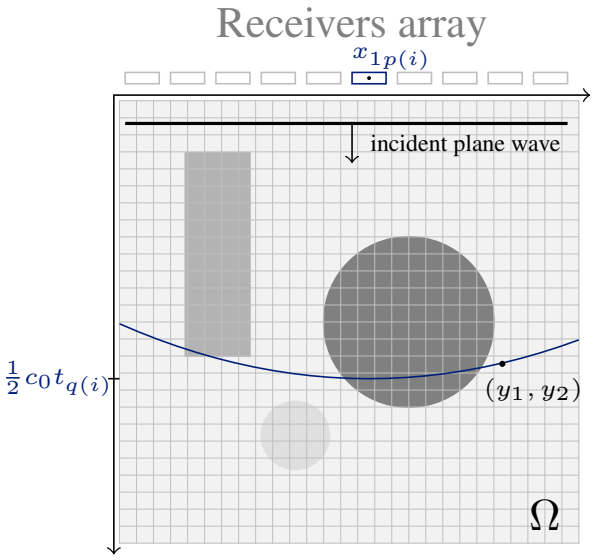

Figure 3.1: Configuration of the plane wave ultrasound imaging. The receivers are located along the x_1 axis and the image domain Ω is discretized uniformly into *pixels* in order to approximate the reflectivity by (3.1.11). The blue solid curve is the ith isochrone given by (3.1.13) and corresponds to the measured data at the receiver $x_{1p(i)}$ and time $t_{q(i)}$.

In practice, the data $d(x_1, t)$ in known only at a discrete set of points from physical measurements. We denote by $N_r \in \mathbb{N} \setminus \{0\}$ and $N_t \in \mathbb{N} \setminus \{0\}$ the number of receivers and temporal samples, and by $M = N_r N_t$ the total number of measurements collected at the receiver position

$$x_{1p(i)} = (p(i) - 1/2)\Delta x, \quad \Delta x > 0, \quad p(i) \in [N_r],$$

and time

$$t_{q(i)} = (q(i) - 1/2)\Delta t, \quad \Delta t > 0, \quad q(i) \in [N_t],$$

where $q(i) = (i-1) \mod N_t + 1$ and $p(i) = (i - q(i))/N_t + 1$, so that each pair $(x_{1p(i)}, t_{q(i)})$ is counted by index $i = N_t(p(i)-1) + q(i)$, $i \in [M]$.

According to the argument of the delta distribution in (3.1.6b), the pair $(x_{1p(i)}, t_{q(i)})$ defines a parabola or an isochrone in the image domain Ω, see Figure 3.1, which is given by

$$y_2 = y_2(y_1) = -\frac{y_1^2}{2c_0 t_{q(i)}} + \frac{x_{1p(i)}}{c_0 t_{q(i)}} y_1 - \frac{x_{1p(i)}^2}{2c_0 t_{q(i)}} + \frac{c_0 t_{q(i)}}{2}, \quad (y_1, y_2) \in \Omega. \tag{3.1.13}$$

Let $d_i = d(x_{1p(i)}, t_{q(i)})$, $i \in [M]$. Then from (3.1.6) and (3.1.11) we obtain

$$d_i = \sum_{j \in [N]} \rho_j K_{ij}, \tag{3.1.14}$$

and the linear system

$$d = K\rho, \tag{3.1.15}$$

for vectors $d = (d_1, \ldots, d_M)^T$, $\rho = (\rho_1, \ldots, \rho_N)^T$, and matrix $K \in \mathbb{R}^{M \times N}$ whose elements given by

$$K_{ij} = [\mathcal{K}\psi_j]\,(x_{1p(i)}, t_{q(i)}). \tag{3.1.16}$$

Notice that the matrix element K_{ij} is equal to the intersection length of the ith isochrone with the jth pixel, and as a result the matrix K is sparse. Hence, to form an image we need to solve the linear system (3.1.15) for the reflexivity vector ρ.

3.1.4 Image Reconstruction

A straightforward approach to solve (3.1.15) is using least squares minimization, where the reflectivity is obtained by minimizing a quadratic objective function

$$\rho^* = \arg\min_{\rho} \|K\rho - d\|_2^2. \tag{3.1.17}$$

The minimizer of (3.1.17) with the smallest ℓ_2 norm can be computed via $\rho^* = K^\dagger d$, where $K^\dagger$ is the pseudo-inverse of K. On the other hand, the Delay and Sum method in Section 3.1.2 evaluates the reflectivity via

$$\rho^*_{DAS} = K^T d, \tag{3.1.18}$$

where K^T denotes the transpose of K. Since for large matrices K, the operator $K^\dagger$ can be ill-conditioned, it makes sense to add a regularization term to the cost function. The standard technique is to consider Tikhonov regularization by adding a quadratic penalty term

$$\rho^*_{l_2} = \arg\min_{\rho} \|K\rho - d\|_2^2 + \lambda\|\rho\|_2^2, \tag{3.1.19}$$

where the weight $\lambda > 0$ provides a trade-off between the data fidelity and smoothness of the solution. To give preference to sparse solutions, we also consider the basic pursuit denoising problem

$$\rho_{l_1}^* = \arg\min_{\rho} \|K\rho - d\|_2^2 + \lambda\|\rho\|_1, \quad \lambda > 0, \tag{3.1.20}$$

where the regularization parameter controls the sparsity of the solution.

3.2 Experiments

In this section we present the reconstruction results for two data sets:

1. synthetic data from the PICMUS dataset [LRMC+16] generated with Field II [Jen96, JS92] in a realistic ultrasound imaging scenario and,

2. *in vitro* Echo PIV data.

The unconstrained minimization problems (3.1.17), (3.1.19) and (3.1.20) are solved numerically using LSQR and YALL1 [YZ11] packages in MATLAB.

3.2.1 Synthetic data

In this part we compare the reconstruction approacher described in Section 3.1.4. Figure 3.2 shows the scatterers configuration with the corresponding measurements. The measurements are collected at N_r =128 receivers and N_t =1353 temporal points. The background speed of sound is set to c_0 =1540 m/s and the image domain measures 38 mm $\times$ 50 mm. The image domain is discretized by a regular grid of size $N = n_1 \times n_2 = 387 \times 676$. Hence, the $M \times N = 173184 \times 261612$ matrix K is underdetermined. Due to the large scale of the problem, we simplify the definition (3.1.16), and set

$$K_{ij} = \begin{cases} 1, & \text{if the } i\text{th isochrone intersects } j\text{th pixel,} \\ 0, & \text{otherwise,} \end{cases} \tag{3.2.1}$$

for all $i \in [M]$ and $j \in [N]$.

In Figure 3.3 we present the reconstruction results for reflectivity vector on absolute scales. We note that all methods visually recover the location of scatterers with good precision. In particular, by choosing a sparsity promoting regularized we reduce the strength of the sidelobes around the scatterers which are visible if we plot reconstruction of logarithmic scale, see Figure 3.4.

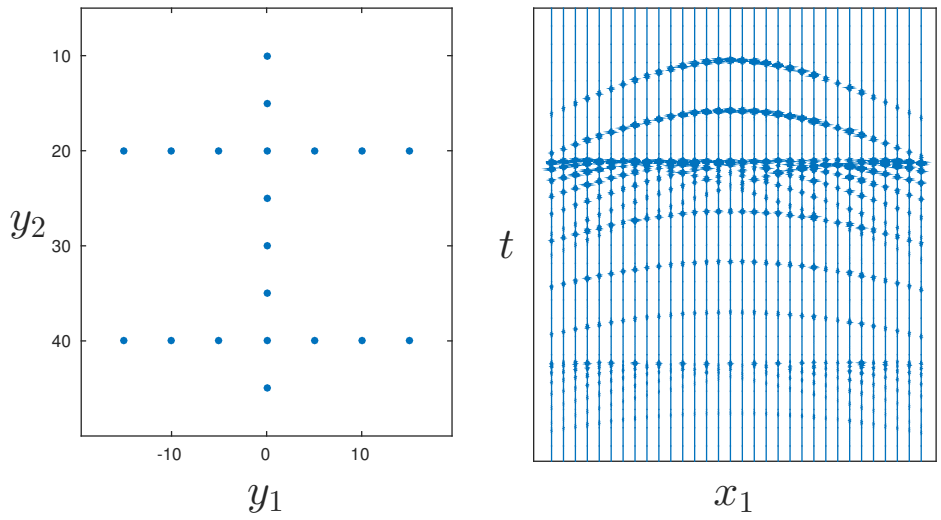

Figure 3.2: LEFT: The configuration of scatterers distributed horizontally and vertically in a homogeneous medium. In the simulation setup, a linear array located at $(y_1, 0)$ transmits an incident plane wave pulse and receives the backscatterd waves which we assume to propagate with constant speed c_0. RIGHT: Time dependent data $d(x_1, t)$ measured at the receiver array. Notice the hyperbolic patterns in the backscattered field due to the isolated scatterers and the decreasing amplitude in the signal for waves traveling longer distances through the medium.

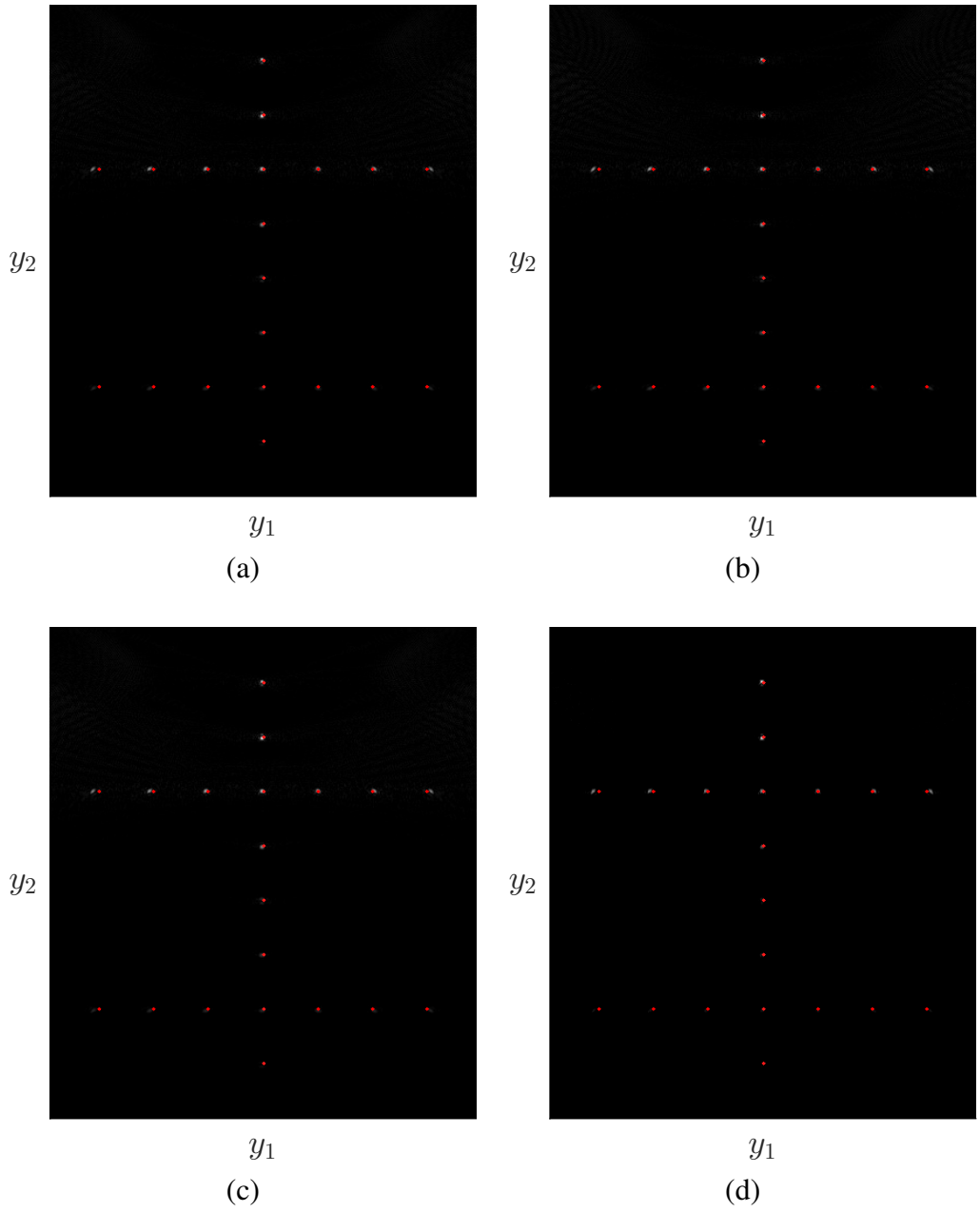

Figure 3.3: Reconstruction of the reflectivity vector with (a) least squares minimization (3.1.17), (b) Delay and Sum (3.1.18), (c) least squares with ℓ_2 regularization (3.1.19), $\lambda = 1$, and (d) basic pursuit denoising (3.1.20), $\lambda = 4$, . Here, we show the absolute value of the reflectivity. The exact location of the scatterers is indicated with small red dots. We observe that all methods are give comparable visual results and that deep scatterers can not be recovered due to the weak backscattered signal. However, the difference between the sparsity promoting approach and other methods is better observed on logarithmic scale shown in Figure 3.4.

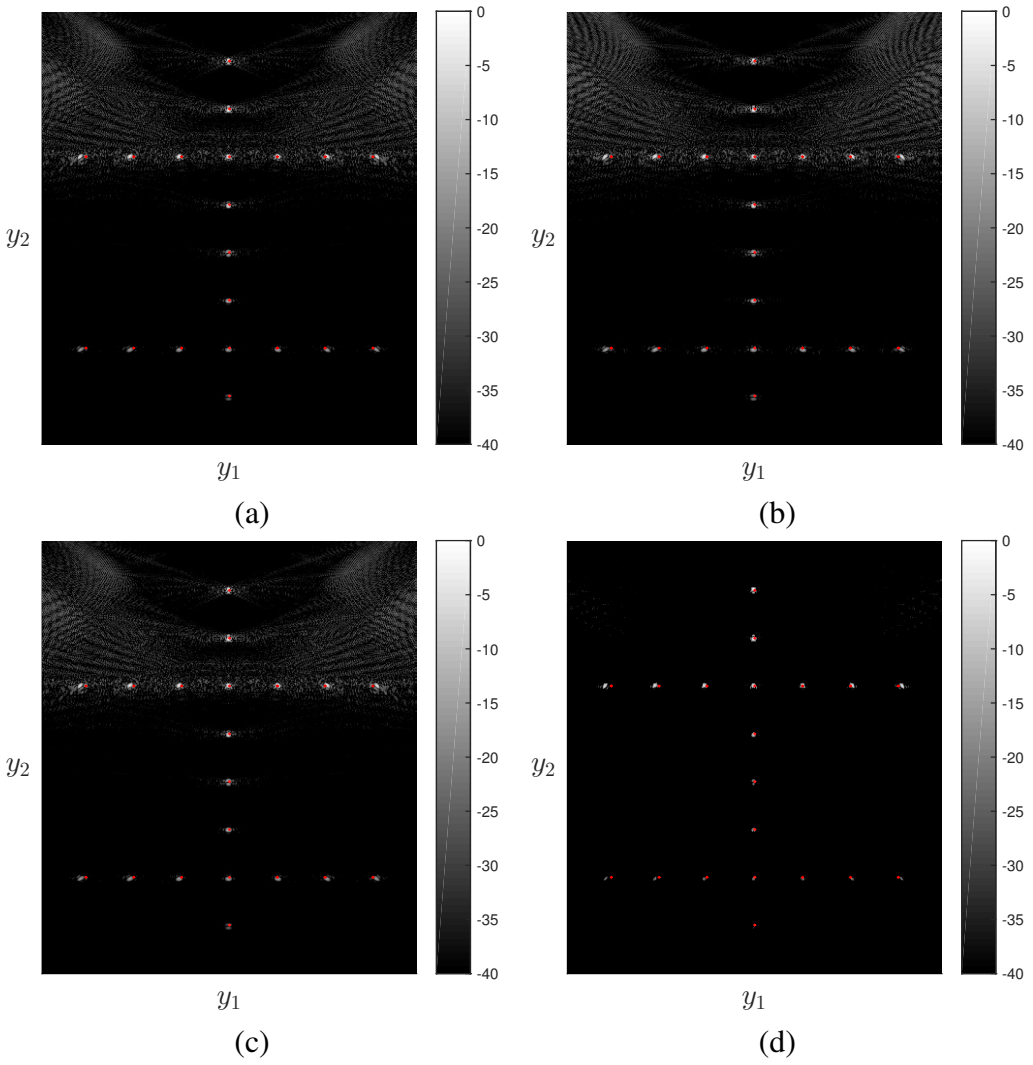

Figure 3.4: Reconstruction of the reflectivity vector with (a) least squares minimization (3.1.17), (b) Delay and Sum (3.1.18), (c) least squares with ℓ_2 regularization (3.1.19), $\lambda = 1$, and (d) basic pursuit denoising (3.1.20), $\lambda = 4$. Here, we show the reflectivity on logarithmic decibel scale (dB) defined by $20 \log_{10}(|\rho| / \max_j |\rho_j|)$ where the absolute value and logarithm are computed component-wise. The exact location of the scatterers is indicated with small red dots. We observe that by promoting sparse solution via ℓ_1 regularization we reduces the side-lobe artifacts around scatterers that are present in other reconstruction methods.

3.2.2 Ultrasound PIV data

In vitro Echo PIV data consists of a sequence of frames probing the motion of tracer particles (gas bubbles) in a static tube, see Section 2.2.2. Typically, the collected 3D data is corrupted by strong reflections coming from rigid tube walls. For the motion estimation task, these signals must be removed to obtain clear images of the moving bubbles. The signal from the static walls can be subtracted out by exploiting its temporal coherence.

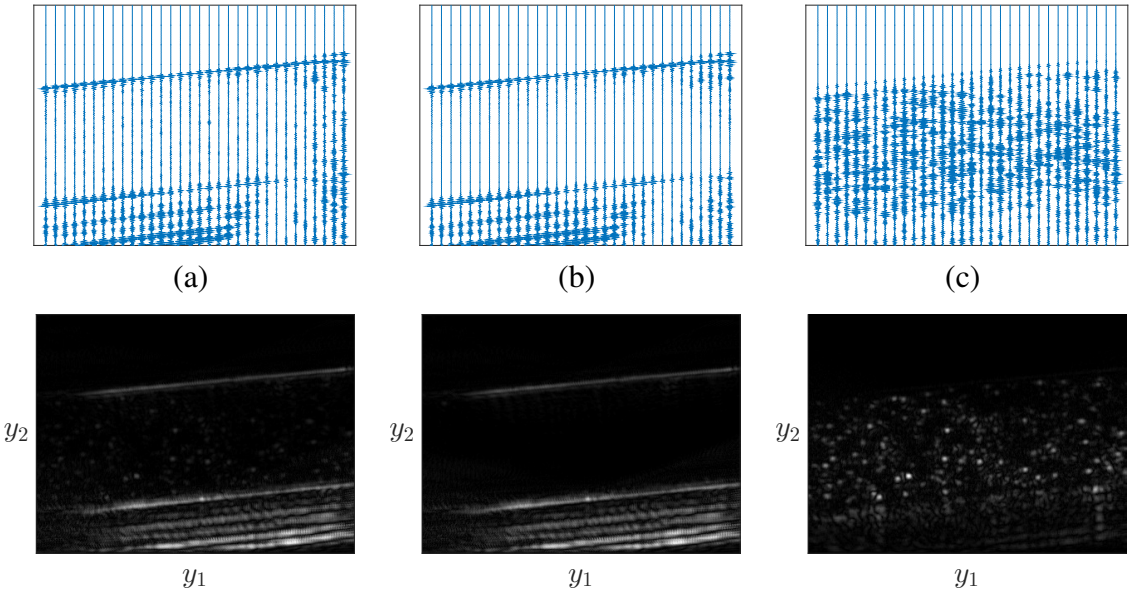

Figure 3.5: Principal component analysis applied to plane wave Echo PIV data. Here, we show a single column from each matrix reshaped into an image. The measured data (a) is decomposed into the strong backscattered signal due to the static and rigid walls (b) and weak backscattered signal coming from the moving bubbles (c). In (d)-(f) we show of the reconstructed image via least square minimizer (3.1.17) in the absolute value scale. The recostructed region is 38 mm wide and reanges from 37 mm to 59 mm in depth. Here, the measured data were multiplied with a time gain compesation factor to acount for depth attenuation effects [Sza04, Chapter 4].

One method to accomplish this, proposed in [DDP+15, AARW17], is to assume that the collected data lie near some low-dimensional subspace. This means, if we stack all temporal frames as columns of the matrix A, then A can be decomposed as

$$A = W + B, \tag{3.2.2}$$

where W is a low-rank matrix corresponding to the stationary signal originating from the walls, and B is a small perturbation which captures the signal due to the moving bubbles. We apply *Principal Component Analysis* (PCA) to find the low-rank matrix

W that solves the minimization problem

$$\min_{W} \|A - W\|_F \quad \text{subject to} \quad \text{rank}(W) \leq k, \tag{3.2.3}$$

where $\|.\|_F$ denotes the Frobenius norm. The minimizer of (3.2.3) can be expressed in terms of the singular values and singular vector of A. For an $m \times n$ matrix A with singular value decomposition

$$A = U\Sigma V^T, \tag{3.2.4}$$

the k-rank matrix solving (3.2.3) is given by

$$W^* = \sum_{i=1}^{k} \sigma_i u_i v_i^T, \tag{3.2.5}$$

where U is an $m \times m$ orthogonal matrix, V is an $n \times n$ orthogonal matrix, Σ is an $m \times n$ diagonal matrix containing the singular values $\sigma_1 \geq \sigma_2 \geq \cdots \geq \sigma_{\min\{n,m\}} \geq 0$, $k \leq \min\{n, m\}$, and u_i and v_i denote the ith column of U and V, respectively.

In Figure 3.5 we shows the resulting decomposition (3.2.2) via (3.2.5) for the *in vitro* Echo PIV data. The measured data contain 299 temporal frames of size $N_r \times N_t$ =128×600, which we stack as columns of the matrix $A \in \mathbb{R}^{76800\times 299}$. For this particular set of data, we notice that $\sigma_1 \gg \sigma_2 \approx \sigma_3$ and therefore set $k = 1$. The signal from the static wall is computed via $W^* = \sigma_1 u_1 v_1^T$ and the signal due to the tracer particles is obtained from $B = A - W^*$. Artifacts due to the Born approximation can be seen in the reconstructed images (d)-(f), where parallel stripes below tube wall are cause by multiple scattering effects.

Chapter 4

Dictionary Based Flow Reconstruction

In this chapter we introduce a *global spatio-temporal* velocimetry technique for laminar and steady pipe flows that extracts the flow model parameter from the entire image sequence. We define a sparse dictionary of particle trajectories parametrized by a single variable and propose to estimate the unknown flow model parameter by using iterative refinement schemes. The approach is validated on synthetic and real, *in-vitro* ultrasound data.

4.1 Recovery Problem

Let f denote the input data, which is a sequence of N_t consecutive temporal frames imaging tracer particles moving with the laminar and steady flow and merged together as shown in Figure 4.1. We assume that f is well-approximated by a superposition of trajectory atoms from a flow dictionary $A(v^*) \in \mathbb{R}_+^{N\times N}$ (that will be introduced in Section 4.1.2) and takes the form

$$f \approx A(v^*)u^*, \tag{4.1.1}$$

where $u^* \in [0,1]^N$ is an indicator vector selecting active trajectories in $A(v^*)$ and $v^* \in \mathbb{R}$ is the flow model parameter corresponding to value of the maximal velocity for laminar and steady pipe flow, see (4.1.4). The model parameter and the indicator vector are unknown and have to be determined from the input data f. To this end we introduce the function

$$J : \mathbb{R}^N \times \mathbb{R} \to \mathbb{R}, \quad J(u,v) := \|A(v)u - f\|_2^2, \tag{4.1.2}$$

and propose to minimize the "distance" between the input data f and the model $A(v)u$ in the least squares sense, i.e. we solve

$$(u^*, v^*) = \arg\min_{(u,v)\in X} \|A(v)u - f\|_2^2, \quad X = [0,1]^N \times [0, v^{(\text{MAX})}], \tag{4.1.3}$$

where $v^{(\text{MAX})}$ is an upper bound for the velocity range, which we assume to be smaller than the resolvable critical velocity for the given temporal resolution of the image

sequence. In other words, we estimate the unknown parameter $v^* \in [0, v^{(\text{MAX})}]$ by adapting a trajectory dictionary $A(v)$ and an indicator vector u to the image sequence f. The sufficient conditions for the convergence on the numerical schemes, employed to solve the nonlinear optimization problem with box constrains (4.1.3), are guaranteed by the continuity and differentiability of the map $v \to A(v)$, discussed in Section 4.1.2.

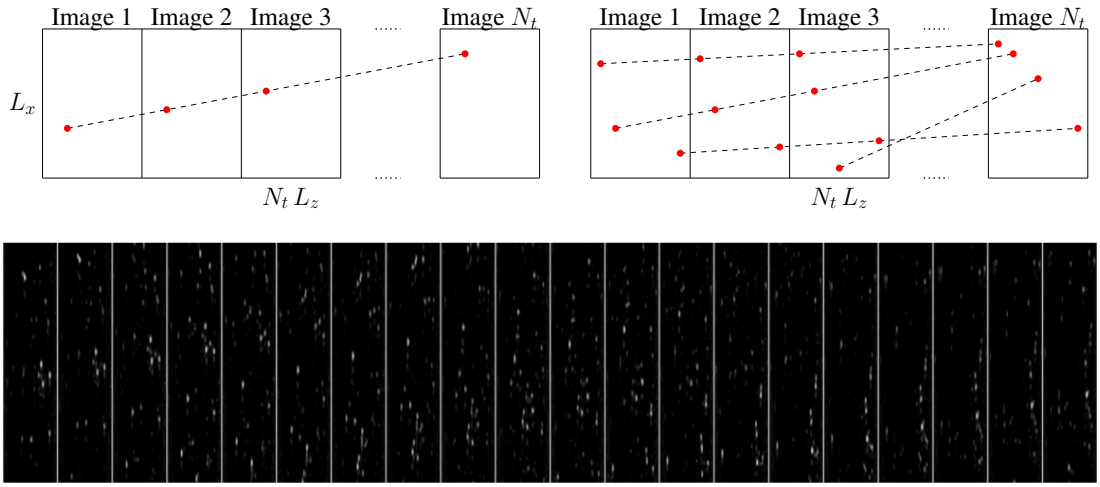

Figure 4.1: TOP ROW: Few temporal frames that illustrate the tracer particles driven by the Poiseuille flow model following linear trajectories. For each particle located at the space-time grid point (x_i, z_j, t_k) we attribute a trajectory defined by the equation of motion (4.1.4) and the model flow parameter v, and assign a column in the dictionary $A(v)$. BOTTOM ROW: Realistic input data f consisting of several noisy frames which display the motion of multiple tracer particles. From such an image sequence we wish to extract the unknown v which parametrizes the flow. In all images the particles move upwards.

4.1.1 Flow Parameter

The laminar and steady flow in a straight cylindrical tube of radius R is governed by the following equations of motion:

$$\begin{cases} x(t) = x(t') + (t - t')\, v_m\, \alpha(z), \\ z(t) = z(t') = const., \end{cases} \tag{4.1.4}$$

where $z \in [0, 2R]$, $\alpha(z) = 1 - (R - z)^2/R^2$ and $t,\ t' \geq 0$. The non-negative parameter v_m is the maximal flow velocity - the velocity of particles moving at the tube center. Subsequently we will omit the index m and denote v_m by v.

4.1.2 Trajectory Matrix

We further detail the construction of the space-time trajectory dictionary $A(v)$, which depends on the maximal flow velocity introduced in (4.1.4). For $L_z = 2R$, let

$$\Omega := [0, L_x] \times [0, L_z] \subset \mathbb{R}^2,$$

denote a fixed field of view in the x/z-plane corresponding to the insonified area inside the tube, see Figure 2.2. We uniformly discretize Ω into $N_x N_z$ rectangular cells

$$\Omega_{i,j} := [(i-1)\,\Delta x, i\,\Delta x] \times [(j-1)\,\Delta z, j\,\Delta z], \qquad i \in [N_x], \quad j \in [N_z] \tag{4.1.5}$$

of size $\Delta x \Delta z$ with $\Delta x = L_x/N_x$, $\Delta z = L_z/N_z$. Using the continuous B-spline basis function of degree one

$$\psi \colon \mathbb{R} \to \mathbb{R}, \qquad \psi(x) := \begin{cases} 2\,x, & 0 \le x < \frac{1}{2}, \\ 2 - 2\,x, & \frac{1}{2} \le x \le 1, \\ 0, & \text{otherwise}, \end{cases} \tag{4.1.6}$$

and the continuously differentiable B-spline basis function of degree three given by

$$\phi \colon \mathbb{R} \to \mathbb{R}, \qquad \phi(x) := \begin{cases} \frac{32}{3}x^3, & 0 \le x < \frac{1}{4}, \\ -\frac{2}{3}(-1 + 12x - 48x^2 + 48x^3), & \frac{1}{4} \le x < \frac{1}{2}, \\ \frac{2}{3}(-11 + 60x - 96x^2 + 48x^3), & \frac{1}{2} \le x < \frac{3}{4}, \\ -\frac{32}{2}(-1 + 3x - 3x^2 + x^3), & \frac{3}{4} \le x \le 1, \\ 0, & \text{otherwise}, \end{cases} \tag{4.1.7}$$

we define for every $(x_i, z_j) = ((i - 1/2)\Delta x, (j - 1/2)\Delta z)$ where

$$(i, j) \in \{-1, 0, \ldots, N_x + 1, N_x + 2\} \times \{0, \ldots, N_z + 1\},$$

the cell-centered 2-dimensional basis functions

$$\varphi_{i,j} \colon \mathbb{R}^2 \to \mathbb{R}, \quad (x, z) \mapsto \varphi_{i,j}(x, z) := \phi_i\Big(\frac{x - x_i}{4\,\Delta x} + \frac{1}{2}\Big)\psi_j\Big(\frac{z - z_j}{2\,\Delta z} + \frac{1}{2}\Big), \tag{4.1.8}$$

that form a partition of unity of Ω. Figure 4.2 (a) and (b) illustrate this property for linear and cubic functions (4.1.6) - (4.1.7) in 1D-domain $[0, L_x]$ with $L_x = N_x = 5$ and $\Delta x = 1$. Note that $N_x + 2$ and $N_x + 4$ basis functions are required for linear and cubic partition, respectively.

A *point particle* located at $(x_0, z_0) \in \Omega$ in a 2D-fluid is *mathematically* represented as a Dirac measure $\delta(x - x_0, z - z_0)$ with unit mass. The *discrete approximation*, $\hat{\delta}_{(x_0,z_0)}(x, z)$, of the Dirac measure is expressed by the corresponding coefficients

$$c_{i,j} = \int_{\mathbb{R}^2} \delta(x_0 - x', z_0 - z')\varphi_{i,j}(x', z')\mathrm{d}x'\mathrm{d}z' = \varphi_{i,j}(x_0, z_0), \tag{4.1.9}$$

with $i \in \{-1, 0, \dots, N_x + 1, N_x + 2\},\ j \in \{0, \dots, N_z + 1\}$ and it takes the form

$$\delta(x - x_0, z - z_0) \approx \hat{\delta}_{(x_0,z_0)}(x, z) = c_{i,j} = \varphi_{i,j}(x_0, z_0), \quad \text{for } (x, z) \in \Omega_{i,j}. \tag{4.1.10}$$

Note that for any $(x_0, z_0) \in \Omega$ the mass of $\hat{\delta}_{(x_0,z_0)}(x, z)$ sums up to one

$$\sum_{i=-1}^{N_x+2} \sum_{j=0}^{N_z+1} \varphi_{i,j}(x_0, z_0) = \underbrace{\sum_{i=-1}^{N_x+2} \phi_i\Big(\frac{x_0 - x_i}{4\,\Delta x} + \frac{1}{2}\Big)}_{=1} \underbrace{\sum_{j=0}^{N_z+1} \psi_j\Big(\frac{z_0 - z_j}{2\,\Delta z} + \frac{1}{2}\Big)}_{=1} = 1, \tag{4.1.11}$$

and the mass of $\hat{\delta}_{(x_0,z_0)}(x, y)$ is no longer concentrated at (x_0, z_0) but "smeared over" the cells containing the location (x_0, z_0) of the point particle and two or three adjacent cells along the x direction, as illustrated in Figure 4.3 (a). This larger, but still focused support of functions representing point particles ensures the sufficient smoothness of the map $v \mapsto A(v)$ that is required for the design of convergent algorithms.

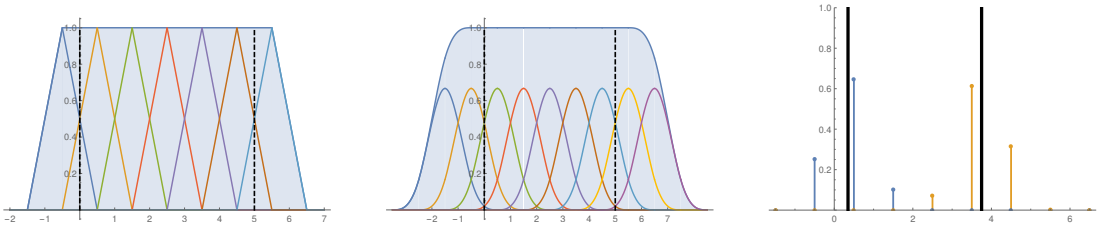

(a) (b) (c)

Figure 4.2: (a) Partition of unity of the domain $[0, 5]$ using the linear B-spline functions (4.1.6). (b) Partition of the domain using cubic B-spline functions (4.1.7). (c) Two unit-mass Dirac measures located at x_1 and x_2, respectively, indicated by the two black lines. The corresponding coefficients $\phi_i(x_1)$ and $\phi_i(x_2)$, for $i \in \{-1, 0, \dots, 7\}$ are indicated by the blue and yellow points, respectively, located at the cell centroids $i - 1/2$.

Regarding the latter matching task, we set up a dictionary of discretized particle trajectories, based on the flow model (4.1.4). Specifically, we consider a sequence of N_t frames imaging the flow within the region Ω at time steps $t_k = (k - 1)\Delta t$, $k \in [N_t]$. The dictionary is composed of all particle trajectories that meet the center positions $(x_i, z_j) = ((i - 1/2)\Delta x, (j - 1/2)\Delta z) \in \Omega_{i,j}$ of all cells given by (4.1.5) for any time t_k, $k \in [N_t]$. Such a dictionary will have the size $N_x N_z N_t \times N_x N_z N_t$.

Let us consider the trajectory of a single particle which is located at (x_i, z_j) at an arbitrary but fixed point of time t_k, $k \in [N_t]$. Due to the flow model (4.1.4), this particle is moving through space-time points

$$\mathcal{T}_{i,j,k} := \Big\{\big(x_{i,k,l},\ z_j,\ t_l\big) : l \in [N_t]\Big\}. \tag{4.1.12}$$

Here, $x_{i,k,l}$ denotes the x-coordinate of the considered particle at time t_l, $l \in [N_t]$, i.e.

$$x_{i,k,l} = x_i + (t_l - t_k) v \alpha(z_j), \tag{4.1.13}$$

and $x_{i,k,k} = x_i$ according to our initial assumption. The union of all such sampled trajectories defines the set of space-time positions

$$\mathcal{T} := \bigcup_{i\in[N_x],j\in[N_z],k\in[N_t]} \mathcal{T}_{i,j,k}. \tag{4.1.14}$$

Each space-time position $(x_{i,k,l}, z_j, t_l) \in \mathcal{T}_{i,j,k} \subset \mathcal{T}$ in (4.1.12) corresponds to a particle $\delta(x - x_{i,k,l}, z - z_j)$, which for the purpose of numerical matching is approximated by

$$\hat{\delta}_{(x_{i,k,l},z_j)}(x, z) = \varphi_{i',j'}(x_{i,k,l}, z_j), \quad \text{for} \quad (x, z) \in \Omega_{i',j'}, \tag{4.1.15}$$

according to (4.1.10).

The final step concerns the definition of a matrix A which collects the coefficients $\varphi_{i',j'}(x_{i,k,l}, z_j)$ corresponding to all functions (4.1.15) indexed by $\mathcal{T}$ of (4.1.14). We first define the auxiliary function

$$\mathrm{ind}\colon (i, j, k) \mapsto (k-1)N_xN_z+(j-1)N_x+i, \quad i \in [N_x],\ j \in [N_z],\ k \in [N_t], \tag{4.1.16}$$

which indexes the collection of N_t cell-discretized domains Ω corresponding to the frames of a given image sequence. We now define the matrix

$$A_{\mathrm{ind}(i',j',l),\mathrm{ind}(i,j,k)} := \varphi_{i',j'}(x_{i,k,l}, z_j) \tag{4.1.17}$$

based on (4.1.15).

In words, each column of A corresponds to the coefficients of the particle approximations (4.1.15) at locations given by $\mathcal{T}_{i,j,k}$ of (4.1.12). For an illustration we refer to Figure 4.3.

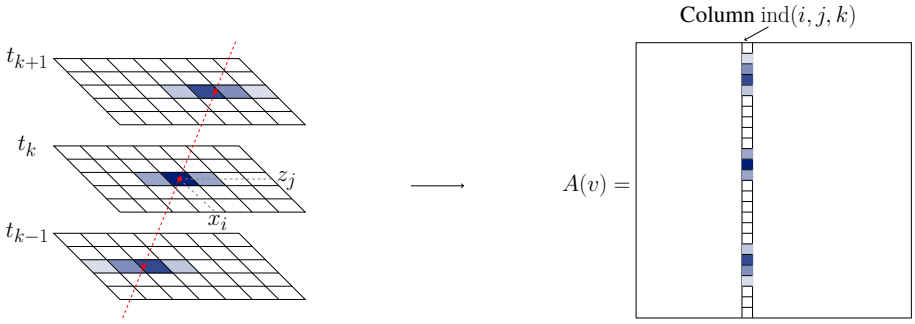

(a) (b)

Figure 4.3: (a) A particle located at (x_i, z_j) at time t_k moves forward or backward to the space-time point $(x_{i,k,k+1}, z_j, t_{k+1})$ or $(x_{i,k,k-1}, z_j, t_{k-1})$, respectively. In the discrete representation, the mass of the particle is no longer concentrated at its space-time point (red dots), rather "smeared over" (blue areas). (b) The index function, $\mathrm{ind}(i, j, k)$ of (4.1.16), defines a column in A with coefficients according to (4.1.17) for all particle locations specified by the set $\mathcal{T}_{i,j,k}$.

Lemma 4.1.1. *The matrix $A \in \mathbb{R}^{N\times N}$, $N = N_x N_z N_t$, defined in (4.1.17) is symmetric.*

Proof. Let $p = \mathrm{ind}(i', j', l)$ and $q = \mathrm{ind}(i, j, k)$, for $i, i' \in [N_x]$, $j, j' \in [N_z]$ and $k, l \in [N_t]$. Plugging (4.1.8) into (4.1.17) we obtain that

$$A_{pq} = \varphi_{i',j'}(x_{i,k,l}, z_j) = \phi_{i'}\left(\frac{x_{i,k,l} - x_{i'}}{4\Delta x} + \frac{1}{2}\right)\psi_{j'}\left(\frac{z_j - z_{j'}}{2\Delta z} + \frac{1}{2}\right), \tag{4.1.18a}$$

$$A_{qp} = \varphi_{i,j}(x_{i',l,k}, z_{j'}, t_k) = \phi_i\left(\frac{x_{i',l,k} - x_i}{4\Delta x} + \frac{1}{2}\right)\psi_j\left(\frac{z_{j'} - z_j}{2\Delta z} + \frac{1}{2}\right). \tag{4.1.18b}$$

Since the basis functions (4.1.6) and (4.1.7) are symmetric and satisfy the relation

$$\psi\left(x + \frac{1}{2}\right) = \psi\left(-x + \frac{1}{2}\right), \tag{4.1.19a}$$

$$\phi\left(x + \frac{1}{2}\right) = \phi\left(-x + \frac{1}{2}\right), \tag{4.1.19b}$$

for all $x \in \mathbb{R}$, we obtain that

$$\psi_{j'}\left(\frac{z_j - z_{j'}}{2\Delta z} + \frac{1}{2}\right) = \psi_j\left(\frac{z_{j'} - z_j}{2\Delta z} + \frac{1}{2}\right). \tag{4.1.20}$$

In particular, for $z_j = (j - 1/2)\Delta z$ and $j \in [N_z]$ we have

$$\psi_{j'}\left(\frac{z_j - z_{j'}}{2\Delta z} + \frac{1}{2}\right) = \psi_j\left(\frac{j - j'}{2} + \frac{1}{2}\right) = \begin{cases} 0 & \text{for } j \neq j', \\ 1 & \text{for } j = j', \end{cases} \tag{4.1.21}$$

since $\psi(x) = 0$ for $x \notin (0, 1)$. Hence, for $j \neq j'$ the function ψ in (4.1.18a) and (4.1.18b) vanishes, implying $A_{pq} = A_{qp} = 0$. For $j = j'$, we have

$$x_{i,k,l} = x_i + (t_l - t_k)v\,\alpha(z_j), \qquad x_{i',l,k} = x_{i'} + (t_k - t_l)v\,\alpha(z_{j'}) \tag{4.1.22}$$

due to (4.1.13), which yields $x_{i,k,l} - x_{i'} = -(x_{i',l,k} - x_i)$ as $z_j = z_{j'}$ and $\alpha(z_j) = \alpha(z_{j'})$. In view of (4.1.19b) and (4.1.18), we obtain that $A_{pq} = \phi_{i'}\left(\frac{x_{i,k,l} - x_{i'}}{4\Delta x} + \frac{1}{2}\right) = \phi_i\left(\frac{x_{i',l,k} - x_i}{4\Delta x} + \frac{1}{2}\right) = A_{qp}$. □

Lemma 4.1.2. *Let $v \in \mathbb{R}_+$ be a non-negative variable representing the flow parameter in (4.1.4). Then (4.1.17) defines a twice continuously differentiable mapping*

$$v \mapsto A(v) \in \mathbb{R}_+^{N\times N}, \quad N = N_x N_z N_t, \tag{4.1.23}$$

with the first and the second derivatives of element A_{pq} given by

$$\dot{A}_{pq}(v) = \frac{\mathrm{d}A_{pq}(v)}{\mathrm{d}v} = \frac{(t_l - t_k)\alpha(z_j)}{4\Delta x}\frac{d\phi_{i'}(\tilde{v})}{d\tilde{v}}\psi_{j'}\left(\frac{z_j - z_{j'}}{2\Delta z} + \frac{1}{2}\right), \tag{4.1.24}$$

$$\ddot{A}_{pq}(v) = \frac{\mathrm{d}^2 A_{pq}(v)}{\mathrm{d}v^2} = \frac{(t_l - t_k)^2\alpha(z_j)^2}{16\Delta x^2}\frac{d^2\phi_{i'}(\tilde{v})}{d\tilde{v}^2}\psi_{j'}\left(\frac{z_j - z_{j'}}{2\Delta z} + \frac{1}{2}\right), \tag{4.1.25}$$

where $p = \mathrm{ind}(i', j', l)$, $q = \mathrm{ind}(i, j, k)$ *for* $i, i' \in [N_x]$, $j, j' \in [N_z]$, $k, l \in [N_t]$,

$$\tilde{v} = \frac{x_i + (t_l - t_k)\alpha(z_j) - x_{i'}}{4\Delta x} + \frac{1}{2}, \tag{4.1.26}$$

and

$$\dot{\phi}(x) = \frac{\mathrm{d}\phi(x)}{\mathrm{d}x} = \begin{cases} 32x^2, & 0 \le x < \frac{1}{4}, \\ -8(12x^2 - 8x + 12x - 1), & \frac{1}{4} \le x < \frac{1}{2}, \\ 4(24x^2 - 32x + 10), & \frac{1}{2} \le x < \frac{3}{4}, \\ -32(x^2 - 2x + 1), & \frac{3}{4} \le x \le 1, \\ 0, & \textit{otherwise}, \end{cases} \tag{4.1.27}$$

$$\ddot{\phi}(x) = \frac{\mathrm{d}^2\phi(x)}{\mathrm{d}x^2} = \begin{cases} 64x, & 0 \le x < \frac{1}{4}, \\ -64(3x - 1), & \frac{1}{4} \le x < \frac{1}{2}, \\ 64(3x - 2), & \frac{1}{2} \le x < \frac{3}{4}, \\ -64(x - 1), & \frac{3}{4} \le x \le 1, \\ 0, & \textit{otherwise}. \end{cases} \tag{4.1.28}$$

Proof. Only the first term of the right-hand side of (4.1.17) depends on v according to (4.1.8) and the equation of motion (4.1.4). By definition, the cubic B-spline function in (4.1.7) is twice continuously differentiable. Hence $A(v)$ is twice continuously differentiable with respect to flow parameter v. Finally, equations (4.1.24) - (4.1.28) follow from the differentiation of (4.1.7).

□

Lemma 4.1.3. *The matrices* $\dot{A} \in \mathbb{R}^{N \times N}$ *and* $\ddot{A} \in \mathbb{R}^{N \times N}$, $N = N_x N_z N_t$, *given by* (4.1.24) *and* (4.1.25) *are symmetric.*

Proof. See the proof of Lemma 4.1.1. □

Corollary 4.1.4. *For* $f \in \mathbb{R}^N$, *the function*

$$J : \mathbb{R}^N \times \mathbb{R} \to \mathbb{R}, \quad J(u, v) := \|A(v)u - f\|_2^2, \tag{4.1.29}$$

is twice continuously differentiable with respect to both variables.

Proof. The differentiability of $J(u, v)$ with respect to variable u is trivial, and the differentiability with respect to v is an immediate consequence of Lemma 4.1.2. □

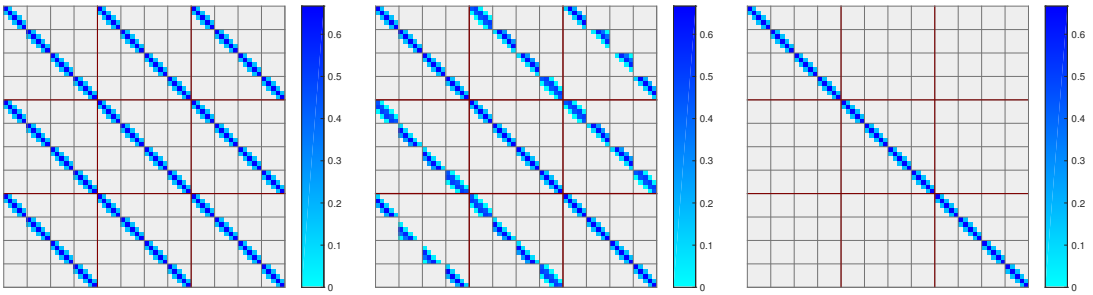

$v = 0$ $\qquad$ $0 < v < v^c$ $\qquad$ $v \geq v^c$

Figure 4.4: Illustration of the matrix $A(v)$ for $N_x = 5$, $N_z = 4$ and $N_t = 3$, where the red vertical and horizontal lines separate submatrices corresponding to different temporal frames. A column in A is determined by a point-particle whose space-time coordinates are specified in (4.1.12). *(Left)* In the motionless scenario, i.e. $v = 0$, the space coordinates remain unchanged over time, resulting in identical patterns for each submatrix. *(Center)* Common representation of $A(v)$ for moderate flow model parameter values, smaller than the resolvable critical velocity v^c given by the temporal resolution of the image sequence. *(Right)* In extreme cases of very large flow maximum velociy, a point particle will be observed at the space-time coordinate (x_i, z_j, t_k) only once and is not visible in other frames.

4.2 Numerical Optimization

In this section we consider the minimization problem

$$\min_{w \in X} J(w), \quad X = [0,1]^N \times [0, v^{(\text{MAX})}], \tag{4.2.1}$$

where the objective function $J(w)$ is given by (4.1.29) and $w = (u^T, v)^T$. We solve the problem by employing the nonmonotone gradient-projection algorithm [BMR00] and the trust region method for constrained optimization problems, extensively discussed in [CGT00, Chapter 12]. The resulting iterative technique produces a sequence of iterates $\{w_k\}$ that converges to a first-order critical point w^* of the problem (4.2.1), i.e.

$$\langle \nabla J(w^*), w - w^* \rangle \geq 0, \quad \forall w \in X. \tag{4.2.2}$$

Our ansatz is to estimate the flow model parameter v^*, from the stationary point

$$w^* = ((u^*)^T, v^*)^T.$$

4.2.1 Spectral Projected Gradient Method

The non-monotone spectral projected gradient (SPG) algorithm [BMR00] is a numerical scheme for minimization of differentiable functions on nonempty closed and convex sets, that extend the classical projected gradient schemes to include a non-monotone steplength strategy. The algorithm works as follows. For the current iterate $w_k \in X$, the new trial iterate is given by

$$w_+ = P_X(w_k - \lambda_k \nabla J(w_k)), \tag{4.2.3}$$

where $P_X(w)$ denotes the unique projection of the vector w on X, $\nabla J(w_k)$ denotes the gradient of J at the point w_k, and $\lambda_k \geq 0$ denotes the step size. The new iterate is accepted and set to $w_{k+1} = w_+$ if the non-monotone Armijo condition

$$J(w_+) \leq \min_{0 \leq j \leq \kappa} J(w_{k-j}) + \gamma \langle \nabla J(w_k), w_+ - w_k \rangle, \tag{4.2.4}$$

is satisfied, where $\gamma \in (0, 1)$ is a sufficient decrease parameter, $\kappa = \min\{k, M - 1\}$ and $M \in \mathbb{N}$ is the non-monotone parameter. If the condition (4.2.4) fails, the step size λ_k is decreased and a new point is generated via (4.2.3). The steps in (4.2.3) and (4.2.4) are repeated until the stopping criteria

$$\|P_X(w_k - \nabla J(w_k)) - w_k\| \leq \varepsilon$$

is met for small $\varepsilon > 0$. Due to Theorem 2.3 in [BMR00] the algorithm is well defined and has the property that every accumulation point of the resulting sequence $\{w_k\}$ is a constrained stationary point that satisfies (4.2.2).

4.2.2 Trust Region Method

The trust region method (TRM) is the second algorithmic strategy implemented to solve (4.2.1). A basic trust-region algorithm works as follows. At each iterate w_k, we construct a model function $m_k(w_k)$ that approximates the actual objective function J within a suitable neighborhood of w_k, i.e. trust region, given by We choose a quadratic model of the form

$$m_k(w_k + s) = J_k(w_k) + \langle \nabla J_k(w_k), s \rangle + \frac{1}{2} \langle s, \nabla^2 J_k(w_k) s \rangle, \tag{4.2.5}$$

so that m_k and J are in agreement up to second order, namely

$$m_k(w_k) = J(w_k), \quad \nabla m_k(w_k) = \nabla_k J(w_k), \quad \nabla^2 m_k(w_k) = \nabla^2 J(w_k). \tag{4.2.6}$$

and the trust region

$$\mathcal{B}_k = \{w \in \mathbb{R}^n \, : \, \|w - w_k\|_2 \in \Delta_k\}, \tag{4.2.7}$$

where Δ_k is called the trust-region radius. Next, we search for an approximate minimizer of the model function and a trail step s_k by solving the subproblem

$$s_k = \arg\min_{\|s\| \in \Delta_k} m_k(w_k + s) \quad \text{such that} \quad w_k + s_k \in X. \tag{4.2.8}$$

A trail point $w_k + s_k$ that approximately minimizes the model is located on the projected-gradient path. This point is called the generalized Cauchy point and is given by

$$w_k^{GC} = w_k + s_k = P_X[w_k - t_k \nabla m_k(w_k)]. \tag{4.2.9}$$

Here, $t_k > 0$ satisfies a set of conditions that ensure a sufficient model decrease within the trust-region. Having determined the trail point, we compute the objective function at w_k^{GC}, and compare it with the value predicated by the model. If the candidate w_k^{GC} does not produce a sufficient decrease in J, we conclude that the trust region is too large, and we shrink it and solve (4.2.8) again. If the sufficient reduction predicted by the model is realized by the objective function, the trail point is accepted as the next iterate and the trust region is expanded or kept the same. For a set of assumptions (that are fulfilled in problem (4.2.1)), the convergence to first-order critical points of the trust region algorithm with convex constraints is shown in [CGT00, Section 12.2.2].

4.2.3 Parametric and Univariate Optimization

If we would know the maximal velocity v^* of the flow profile, then we could approximatively tracer particles along trajectories by determining the indicator vector u^* via

$$u^* = \arg\min_{u \in [0,1]^N} \|A(v^*)u - f\|_2^2. \tag{4.2.10}$$

This idea suggests that we should consider the function

$$g : [0, v^{(\text{MAX})}] \to \mathbb{R}_+, \quad g(v) = \min_{u \in [0,1]^N} \|A(v)u - f\|_2^2, \tag{4.2.11}$$

and assume that the minimizer of $g(v)$ provides an estimate of the unkown flow parameter v^*. In the following, we recast (4.2.1) as a parametric optimization problem of the form

$$(P_v) \qquad \min_{u \in \mathbb{R}^N} J(u, v) \qquad \text{s.t.} \quad u \in F(v), \tag{4.2.12}$$

where $J(u, v) : \mathbb{R}^N \times \mathbb{R} \to \mathbb{R}$, $J(u, v) := \|A(v)u - f\|_2^2$ and $F(v) := [0, 1]^N$ is the *constant* feasible set and thus independent of v. Then g from (4.2.11) is the *optimal value function* of (4.2.12), given by $g(v) = \min_{u \in F(v)} J(u, v)$. We denote by $S(v) = \arg\min_{u \in F(v)} J(u, v)$ the optimal solution set and investigate continuity of $v \mapsto g(v)$ and the associated set valued mapping $v \rightrightarrows S(v)$. Continuity of g is a minimal requirement for reliable numerical optimization.

Theorem 4.2.1. *[BS00, Prop. 4.4] Let $v_0 \in \mathbb{R}$ be an arbitrary point in the parameter space. Suppose that*

(i) the function $(u, v) \mapsto J(u, v)$ is continuous on $\mathbb{R}^N \times \mathbb{R}$,

(ii) the multifunction $v \rightrightarrows F(v)$ is closed,

(iii) there exist an $\alpha \in \mathbb{R}$ and a compact set $K \subset \mathbb{R}^N$ such that for every v in a neighborhood of v_0, the level set

$$\operatorname{lev}_\alpha J(\cdot, v) := \{u \in F(v) \ : \ J(u, v) \leq \alpha\} \tag{4.2.13}$$

is nonempty and contained in K,

(vi) for any neighborhood $\mathcal{V}_u$ of the set $S(v_0)$ there exists a neighborhood $\mathcal{V}_v$ of v_0 such that $\mathcal{V}_u \cap F(v) \neq \varnothing$ for all $v \in \mathcal{V}_v$.

Then the optimal value function $g(v)$ is continuous at $v = v_0$, and the multifunction $v \rightrightarrows S(v)$ is upper semi-continuous at v_0.

Corollary 4.2.2. *The optimal value function $g(v)$ from (4.2.11) is continuous on $\mathbb{R}$.*

Proof. We apply Theorem 4.2.1. *(i)* holds since J is continuous in both arguments in view of the definition of J and the continuity of $v \mapsto A(v)$ by Lemma 4.1.2. *(ii)* and *(iv)* hold automatically since the feasible set $F(v) = [0, 1]^N$ is constant and closed. Finally, *(iii)* holds since for any $v \in \mathbb{R}$ the solution set $S(v)$ is nonempty in view of the compactness of the feasible set and continuity of $J(\cdot, v)$. Hence $\forall \alpha \geq g(v) \in \mathbb{R}$ we have $\varnothing \neq S(v) \subset \operatorname{lev}_\alpha J(\cdot, v) \subset [0, 1]^N =: K$. □

A straightforward way of approximating the minimizer of $g(v)$ from (4.2.11) in the interval $0 \leq v \leq v^{(\text{MAX})}$ would be to evaluate the function at a fine grid of points in $[0, v^{(\text{MAX})}]$ and choose the one corresponding to the lowest value, as illustrated in Figure 4.5. Alternatively , we can solve the problem

$$\min_{v \in [0, v^{(\text{MAX})}]} g(v), \tag{4.2.14}$$

using the algorithm proposed in [MS93], where the authors presented a rapidly converging five-point algorithm closely related to the well-known bisection method [Min89] for *continuous* univariate functions, which uses function evaluations, but no derivatives. The method uses function values at five points, denoted and ordered such that

$$\hat{v}_- < v_- < v_0 < v_+ < \hat{v}_+, \tag{4.2.15}$$

to construct quadratic and polyhedral approximations to the function and then choose a point among the minimizers of the approximating functions via rules that do not require additional function evaluations. We refer to the original paper [MS93] for further details and the convergence analysis of the five-point algorithm.

4.3 Experiments

We implemented the nonmonotone spectral projected gradient algorithm (SPG), trust region method (TRM) and five point algorithm (for univariate minimization) to estimate the flow model parameter for two data sets. The first data set is a synthetic, noise free, small size image sequence of tracer particles transported by a Poiseuille flow. The second set is a real, noisy *in-vitro* Echo PIV image sequence.

	$L_z = 2R$	L_x	Δt	N_t	$N_x \times N_z$	$N = N_x N_z N_t$
Synthetic data	0.5 cm	4 cm	1/750 s	10	30×30	900
Ultrasound data	0.5 cm	4 cm	1/6667 s	10	372×135	502200

Table 4.1: The data set parameters used in the experiments. For N_t temporal frames of size $N_x \times N_z$ the input data vector f and the sparse trajectory matrix $A(v)$ have the dimension N and $N \times N$, respectively, which for large-scale problems can be computationally prohibitive.

In Table 4.1 we provide the relevant parameters for both data sets. In addition, we implemented the projected gradient algorithm within the framework of SPG with a monotone steplength strategy, which corresponds to $M = 1$. In the numerical experiments we used the default parameters for SPG and TRM as specified in the original works [BMR00] and [CGT00], respectively. We used the same initial iterate for all minimization schemes. The performance of all algorithms is illustrated in Figure 4.6 and the estimated model flow parameter are summarized in Table 4.2. We observe that univariate minimization solved with the five point algorithm [MS93] significantly outperforms SPG and TRM with respect to number of iteration required to attain the minimum of the objective function and hence to obtain a fast estimate of the flow model parameter. As can be seen from Figure 4.6, the algorithm converges in very few iterations even for large scale problems. The formulation of (4.2.1) as an univariate minimization problem is the essential feature of this method.

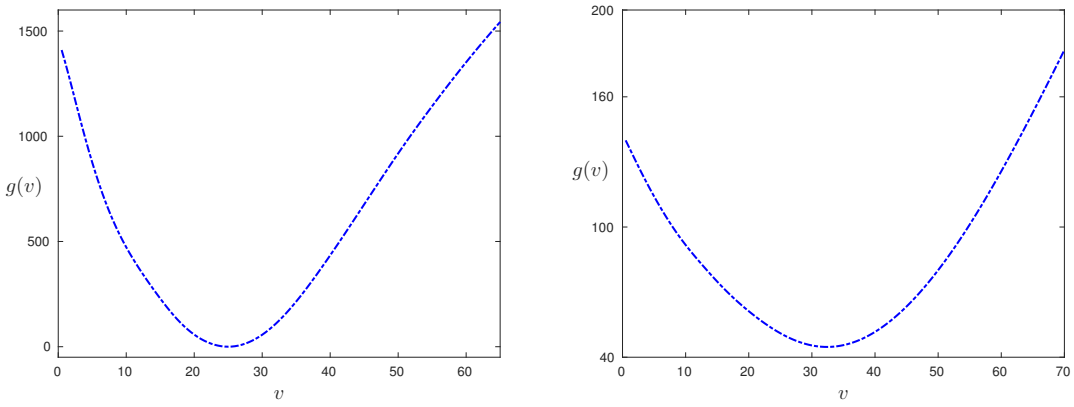

(a) (b)

Figure 4.5: The univariate function $g(v)$ for (a) synthetic and (b) ultrasound data sets. The constrained convex optimization problem (4.2.11) is solved using FISTA [BT09]. The naïve strategy for finding the minimizer of $g(v)$, which provides an estimate of the unknown flow parameter v^*, consists in evaluating the function for a finite set of velocities in an interval $v \in [0, v^{(\text{MAX})}]$ and selecting the argument with the lowest function value. A numerically faster solution scheme is the five point algorithm [MS93] for univariate functions. For numerical results we refer to Table 4.2.

	Synthetic data	Ultrasound data
Reference v^*	25.0	38.2
Naïve $g(v)$ minimization	25.0	32.5
Univariate minimization [MS93]	25.0	32.4
Monotone SPG, $M = 1$	25.1	32.1
Non-monotone SPG, $M = 10$	25.0	32.0
Trust Region Method	25.6	31.8

Table 4.2: The results for model flow parameter v^* (in cm/s) estimated with the proposed numerical schemes. The ground truth maximal flow velocity, i.e. the reference value, is know for synthetic data. For the case of ultrasound data, the reference value was estimated from the volume flow rate and is subject to experimental errors.

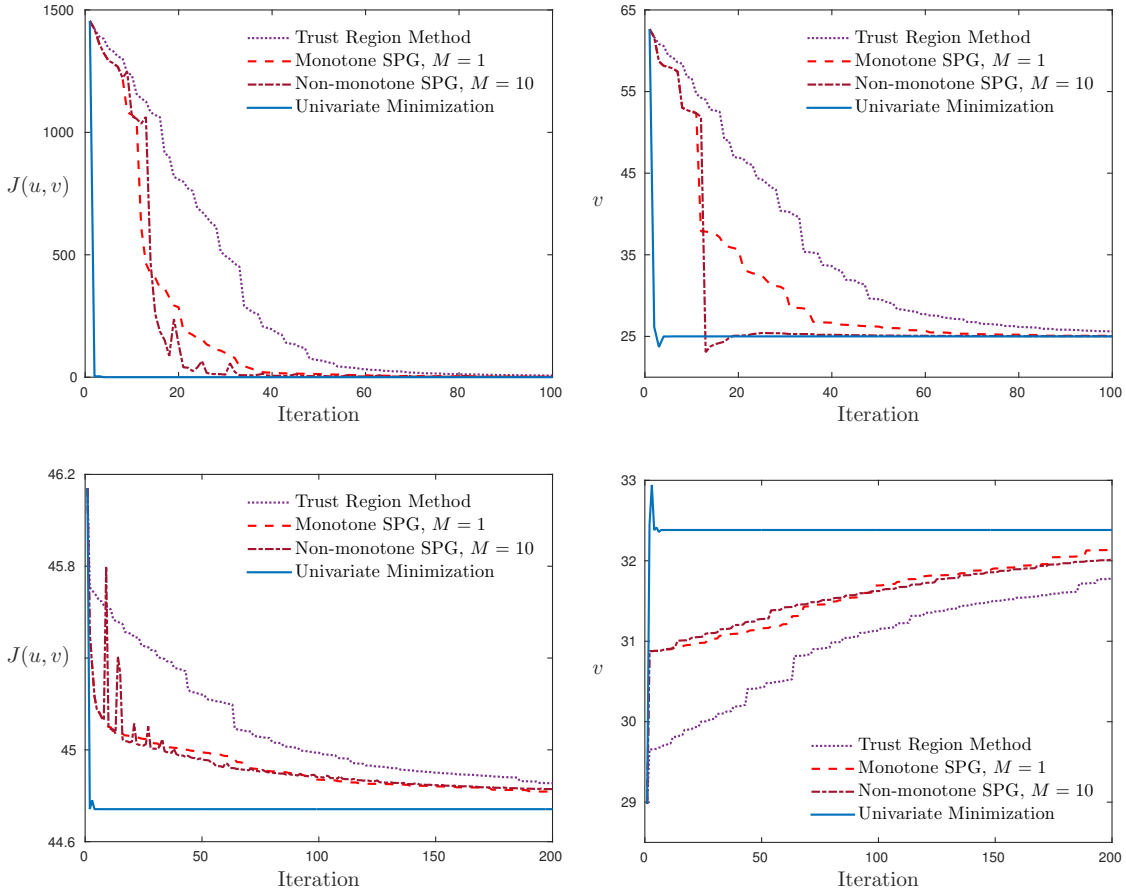

Figure 4.6: Performance of iterative minimization schemes considered to solve the constrained convex optimization problem (4.2.1). TOP ROW: Synthetic data. BOTTOM ROW: Ultrasound data. LEFT: Objective function given in (4.1.29) at each iteration step. RIGHT: Model flow parameter at each iteration step. For the case of noise free synthetic data the optimal value of the objective function (4.2.1) is zero.

Chapter 5

A Spectral Approach to Velocity Estimation

The previous chapter introduced a dictionary based method for estimating the flow parameter v_m under the assumption of the Poiseuille flow model (2.2.1).

In this chapter we continue our study of velocity field estimation from an image sequence function $f(x,t)$. We analyze its spectrum in Fourier domain and approach the problem from two different points of view. The first one is *global* and concerns the overall behavior of the spectrum $\hat{f}(\omega)$ for affine flows. The second view point is *local* and concerns the behavior of the phase component of a filter response function.

5.1 Image Sequence Spectra

The d-dimensional Fourier transform and its inverse are given by

$$\hat{f}(\omega) = \mathcal{F}(f)(\omega) = \int_{\mathbb{R}^d} f(x) e^{-i\langle \omega, x\rangle} \mathrm{d}x, \tag{5.1.1a}$$

$$f(x) = \mathcal{F}^{-1}(\hat{f})(x) = \frac{1}{(2\pi)^d} \int_{\mathbb{R}^d} \hat{f}(w) e^{+i\langle \omega, x\rangle} \mathrm{d}\omega, \tag{5.1.1b}$$

where f is an integrable function, $\langle \omega, x\rangle = \sum_{i\in[d]} \omega_i x_i$ denotes the Euclidean inner product and $[d] := \{1, 2, \ldots, d\}$.

The Fourier transform is an one-to-one mapping on the Schwartz space $\mathcal{S}(\mathbb{R}^d)$ of functions with rapidly decreasing derivatives of any order. It can be extended by duality to the space $\mathcal{S}'(\mathbb{R}^d)$ of tempered distributions, i.e. the space of linear and continuous functionals acting on $\mathcal{S}(\mathbb{R}^d)$. We refer to e.g. [Geo15, Ch. 8.1-3] for details.

The motion of a tracer particle restricted to a 2D imaging plane and driven by laminar and steady pipe flow is governed by the affine equation $x = x_0 + ut$, where $u \in \mathbb{R}^2$ is a time independent velocity and $x_0 \in \mathbb{R}^2$ is a constant initial coordinate. To describe the motion of N_p non-interacting particles we define the image sequence function

$$f(x,t) = \sum_{i\in[N_p]} \delta(x - x^{(i)} - u^{(i)}t), \qquad u^{(i)} = u(x^{(i)}), \tag{5.1.2}$$

where $u^{(i)} = (u_1^{(i)}, 0)^\top$ and $x^{(i)} = (x_1^{(i)}, x_2^{(i)})^\top$ are the time independent velocity and initial position of particle i, respectively, and $u^{(i)}$ is given by (2.2.1) or (2.2.2). Note that the image sequence function $f(x,t)$ is an element of $\mathcal{S}'(\mathbb{R}^3)$, that is a tempered distribution. However, it will be convenient to use the term 'function' for f even if a distribution actually is meant.

Proposition 5.1.1. *Let $\omega = (\omega_x^\top, \omega_3)^\top = (\omega_1, \omega_2, \omega_3)^\top$ denote the angular frequency vector. Then the Fourier transform of the image sequence function (5.1.2) is given by*

$$\hat{f}(\omega) = \hat{f}(\omega_x, \omega_3) = \sum_{i \in [N_p]} e^{-i\langle \omega_x, x^{(i)} \rangle} \delta(\omega_1 u_1^{(i)} + \omega_3). \tag{5.1.3}$$

Proof. Let $h(x) = h(x_1, x_2)$ denote an arbitrary 2D image function. Then, for any fixed vector $u \in \mathbb{R}^2$, the image sequence function $\tilde{h}(x,t) = h(x - ut)$ corresponds to the translation of the function $h(x)$ with constant velocity u. Applying the 3D Fourier transform to this image sequence yields

$$\begin{aligned}
\mathcal{F}(\tilde{h})(\omega) &= \int_{\mathbb{R}^3} h(x - ut) e^{-i(\langle \omega_x, x \rangle + \omega_3 t)} \mathrm{d}x \mathrm{d}t && \text{(5.1.4a)} \\
&= \int_{\mathbb{R}^2} h(z) e^{-i\langle \omega_x, z \rangle} \mathrm{d}z \int_{\mathbb{R}} e^{-i(\langle \omega_x, u \rangle + \omega_3)t} \mathrm{d}t && \text{(5.1.4b)} \\
&= \hat{h}(\omega_x) \delta(\langle \omega_x, u \rangle + \omega_3), && \text{(5.1.4c)}
\end{aligned}$$

where we did a change of variable $z = x - ut$ to obtain (5.1.4b) and the evaluation of the last integral follows from $\delta(\omega) = \int_{\mathbb{R}} e^{-i\omega t} \mathrm{d}t$. Now, setting $h^{(i)}(x) = \delta(x - x^{(i)})$, Eq. (5.1.2) reads

$$f(x,t) = \sum_{i \in N_p} h^{(i)}(x - u^{(i)} t). \tag{5.1.5}$$

Applying relation (5.1.4) and taking into account the linearity of the Fourier transform, we get

$$\begin{aligned}
\hat{f}(\omega) &= \sum_{i \in N_p} \hat{h}^{(i)}(\omega_x) \delta(\langle \omega_x, u^{(i)} \rangle + \omega_3) && \text{(5.1.6a)} \\
&= \sum_{i \in N_p} e^{-i\langle \omega_x, x^{(i)} \rangle} \delta(\langle \omega_x, u^{(i)} \rangle + \omega_3), && \text{(5.1.6b)}
\end{aligned}$$

which due to the specific form of the velocity field $u^{(i)} = (u_1^{(i)}, 0)^\top$, is equal to (5.1.3). □

Equation (5.1.3) states that the spectrum $\hat{f}$ of the image sequence f is the sum of complex phase functions on a corresponding pencil of planes through the origin $\omega = 0$ with normal vectors $n^{(i)} = (u_1^{(i)}, 0, 1)^\top$. Figure 5.1 depicts the resulting support of $\hat{f}(\omega)$, which is bounded by two extremal planes corresponding to zero velocity $u = 0$ with normal $(0, 0, \omega_3)^T$, and to the peak velocity $u = (v_m, 0)^\top$ with normal $(v_m, 0, 1)^\top$, where $v_m = \max_{i \in [N_p]} u_1^{(i)}$.

This observation suggests to determine the peak velocity v_m by estimating the *spectral support* of the Fourier transform of a given image sequence.

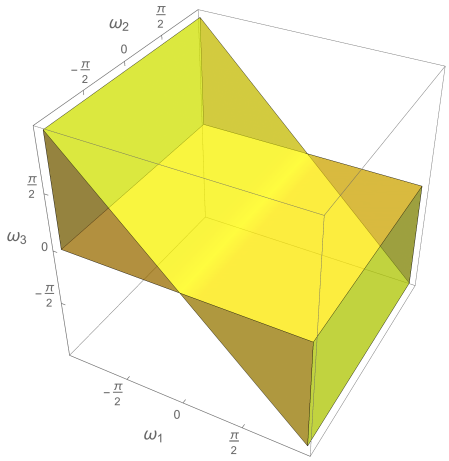

Figure 5.1: Spectral support of the Fourier transform of an image sequence corresponding to the pipe flow model. This non-pointed cone, that extends along the ω_2 axis, is bounded by two planes, namely $\omega_3 = 0$ and $v_m\omega_1 + \omega_3 = 0$. The normal vector of the other plane depends on the unknown peak velocity v_m that we wish to estimate from image sequence data.

5.2 Peak Velocity Estimation

In the following we derive a piecewise linear model of the cone geometry depicted in Figure 5.1 that takes into account noise suppression and the symmetry of real signals in the complex Fourier domain. Based on this model, we develop a numerical method for estimating the spectral support, and hence, the unknown v_m.

5.2.1 Direct Spectral Support Estimation

The cone shown in Figure 5.1 is bounded by the box $[-\pi, \pi]\times[-\pi, \pi]\times[-\pi, \pi]$ and the planes $\omega_3 = 0$, $v_m\omega_1 + \omega_3 = 0$. Due to the high noise level of real data, we discard the spectrum at large frequencies as well as a redundant half-space due to the symmetry of real signals $f(x, t)$ in Fourier space. As a consequence, we only consider the spectrum in the smaller box $[0, \pi/4]\times[-\pi/4, \pi/4]\times[-\pi/4, 0]$. Assuming a uniform distribution of the amplitude spectrum

$$|\hat{f}(\omega)| \approx C_f, \tag{5.2.1}$$

of the image sequence signal $f(x, t)$ for some constant $C_f > 0$, we define the region

$$\Omega(v) = \left\{\omega \in \mathbb{R}^3 \colon 0 \le \omega_1 \le \frac{\pi}{4},\ -\frac{\pi}{4} \le \omega_2 \le \frac{\pi}{4},\ -\min\left\{v\,\omega_1, \frac{\pi}{4}\right\} \le \omega_3 \le 0\right\}, \tag{5.2.2}$$

for $v \ge 0$ and estimate the spectral support of $\hat{f}$ by the volume integral

$$s(v) = \frac{1}{|\Omega(v_m)|}\int\limits_{\Omega(v)} |\hat{f}(\omega)|\mathrm{d}\omega, \qquad v_m, v > 0. \tag{5.2.3}$$

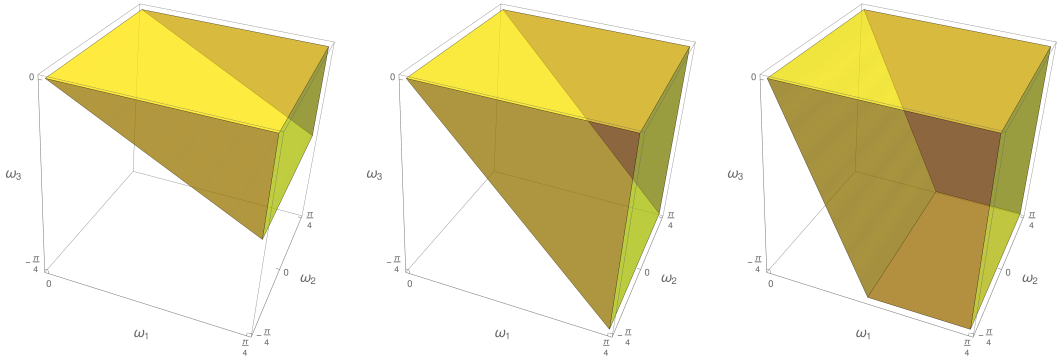

(a) (b) (c)

Figure 5.2: This figure illustrates the set $\Omega(v_m)$ that defines the spectral support of $\hat{f}$ for (a) $v_m < 1$, (b) $v_m = 1$, and (c) $v_m > 1$. Conversely, estimating the actual support for a given spectrum $\hat{f}$ corresponding to real image sequence data f, enables to estimate the parameter v_m.

Because the support of $|\hat{f}(\omega)|$ is restricted to $\Omega(v_m)$, the volume integral attains its maximum for $v \geq v_m$, in which case $s(v) = C_f$. The geometry of the set $\Omega(v_m)$, illustrated in Figure 5.2, suggests to distinguish between the following two cases for the analytical evaluation of $s(v)$.

Case 1: If $v_m \leq 1$, then $|\Omega(v_m)| = \left(\frac{\pi}{4}\right)^3 v_m$ and (5.2.3) takes the form of a piecewise linear function with one breakpoint at v_m

$$s(v) = \begin{cases} \frac{C_f}{v_m} v, & 0 \leq v < v_m, \\ C_f, & v \geq v_m. \end{cases} \tag{5.2.4}$$

This case is illustrated in Figure 5.2 (a) and (b).

Case 2: If $v_m > 1$, then $|\Omega(v_m)| = \left(\frac{\pi}{4}\right)^3 (2 - \frac{1}{v_m})$ and (5.2.3) is given by

$$s(v) = \begin{cases} \frac{C_f}{2-\frac{1}{v_m}} v, & 0 \leq v < 1, \\ \frac{C_f}{2-\frac{1}{v_m}} (1 - \frac{1}{v}), & 1 \leq v < v_m, \\ C_f, & v \geq v_m, \end{cases} \tag{5.2.5}$$

which is a piecewise non-linear function with breakpoints at 1 and v_m. This case is illustrated in Figure 5.2 (c).

In practice we can compute $\hat{f}(\omega)$ from the image sequence $f(x,t)$ using Fast Fourier Transform (FFT) and then evaluate $s(v)$ numerically as a Riemannian sum that approximates (5.2.3). Equations (5.2.4) and (5.2.5) suggest that one breakpoint of $s(v)$ corresponds to v_m, that we wish to estimate.

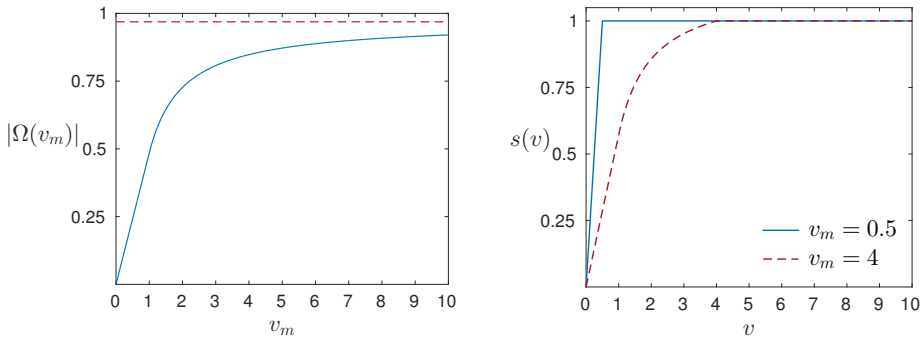

Figure 5.3: (Left) The dependence $|\Omega(v_m)|$ on v_m. The red dashed line is the upper bound of $|\Omega(v_m)|$ as $v_m \to \infty$ that equals $\pi^3/32$. (Right) The normalized function $s(v)$ for case 1 when $v_m < 1$ and case 2 when $v_m > 1$.

5.2.2 Parameter Estimation

We first develop *smooth* parametric representations of (5.2.4) and (5.2.5) that are amenable to efficient numerical optimization, followed by sketching the numerical approach for evaluation of the piecewise linear/non-linear fitting.

5.2.2.1 Piecewise Linear Model

Equation (5.2.4) suggests that the data set $\{\hat{v}_i, s(\hat{v}_i)\}_{i\in[n]}$ estimated numerically from (5.2.3) via the Riemannian sum is best approximated by a two-segment piecewise linear continuous function of the form

$$g : \mathbb{R} \mapsto \mathbb{R}, \quad g(x) = \begin{cases} a_1 + b_1 x, & x \le \xi, \\ a_2 + b_2 x, & x > \xi. \end{cases} \tag{5.2.6}$$

We define

$$l_1(x) = a_1 + b_1 x, \quad l_2(x) = a_2 + b_2 x, \tag{5.2.7}$$

and rewrite (5.2.6) as

$$g(x) = -\max\{-l_1(x), -l_2(x)\}. \tag{5.2.8}$$

A *smooth* approximation of $g(x)$ can be achieved by using the log-exponential function,

$$g_\varepsilon(x) = -\varepsilon \ln\left(\mathrm{e}^{-l_1(x)/\varepsilon} + \mathrm{e}^{-l_2(x)/\varepsilon}\right), \tag{5.2.9}$$

where $\varepsilon > 0$ is the smoothing parameter that enables a *uniform* approximation, to any accuracy, of (5.2.8) as $\varepsilon \to 0$ [RW09, Ch. 1.-H].

From (5.2.7) and the continuity of $g(x)$ at the breakpoint ξ, which implies that $a_1 + b_1\xi = a_2 + b_2\xi$, we can express (5.2.9) as

$$g_\varepsilon(x) = -\varepsilon \ln\left(\mathrm{e}^{-(a_1+b_1x)/\varepsilon} + \mathrm{e}^{-(a_1+(b_1-b_2)\xi+b_2x)/\varepsilon}\right) \tag{5.2.10a}$$

$$= \alpha + \beta x - \varepsilon \ln\left(1 + \mathrm{e}^{-\gamma(x-\xi)/\varepsilon}\right), \tag{5.2.10b}$$

where

$$\alpha = a_1, \quad \beta = b_1, \quad \text{and} \quad \gamma = b_2 - b_1. \tag{5.2.11}$$

5.2.2.2 Piecewise Non-Linear Model

In view of (5.2.5) we consider the piecewise non-linear continuous function

$$h(x) : \mathbb{R}_+ \setminus \{0\} \mapsto \mathbb{R}, \quad h(x) = \begin{cases} a_1 + b_1 x, & 0 < x \le \xi_1, \\ a_2 + \frac{b_2}{x}, & \xi_1 < x \le \xi_2, \\ a_3 + b_3 x, & x > \xi_2, \end{cases} \tag{5.2.12}$$

where $0 < \xi_1 \le \xi_2$ are the breakpoints.

Lemma 5.2.1. *For two breakpoints $0 < \xi_1 \le \xi_2$ the function defined in (5.2.12) has the canonical representation*

$$h(x) = \alpha + \beta x + \sum_{i\in[2]} \delta_i \left|\frac{1}{x} - \frac{1}{\xi_i}\right| + \sum_{i\in[2]} \phi_i |x - \xi_i| \tag{5.2.13}$$

where

$$\alpha = \frac{a_1 + a_3}{2}, \ \beta = \frac{b_1 + b_3}{2}, \ \delta_1 = -\delta_2 = -\frac{b_2}{2}, \ \phi_1 = -\frac{b_1}{2}, \ \textit{and} \ \phi_2 = \frac{b_3}{2}. \tag{5.2.14}$$

Proof. The result follows immediately from the continuity of $h(x)$ at the breakpoints ξ_1, ξ_2 and the expansion of absolute value terms for the cases $0 < x \le \xi_1$, $\xi_1 < x \le \xi_2$ and $x > \xi_2$. □

Lemma 5.2.2. *The piecewise non-linear function (5.2.13) can be approximated uniformly by the smooth function*

$$h_\varepsilon(x) = A + Bx + \sum_{i\in[2]} D_i \ln\left(1 + \mathrm{e}^{-2\left(\frac{1}{x} - \frac{1}{\xi_i}\right)/\varepsilon}\right) + \sum_{i\in[2]} F_i \ln\left(1 + \mathrm{e}^{-2(x-\xi_i)/\varepsilon}\right), \tag{5.2.15}$$

where $A = \alpha - \delta_1/\xi_1 - \delta_2/\xi_2 - \phi_1\xi_1 - \phi_2\xi_2$, $B = \beta + \phi_1 + \phi_2$, $D_i = \varepsilon\delta_i$ and $F_i = \varepsilon\phi_i$, for $i \in \{1, 2\}$.

Proof. The absolute value of $x \in \mathbb{R}$ can be expressed as

$$|x| = \max\{-x, x\}, \tag{5.2.16}$$

and, similar to the discussed above, is approximated uniformly by the smooth function

$$|x|_\varepsilon = \varepsilon \ln\left(\mathrm{e}^{-x/\varepsilon} + \mathrm{e}^{x/\varepsilon}\right) = x + \varepsilon \ln\left(1 + \mathrm{e}^{-2x/\varepsilon}\right). \tag{5.2.17}$$

The replacement of the absolute value terms in (5.2.13) with the corresponding smooth approximations $\left|\frac{1}{x} - \frac{1}{\xi_i}\right|_\varepsilon$ and $|x - \xi_i|_\varepsilon$, for $i \in [2]$, yields (5.2.15). □

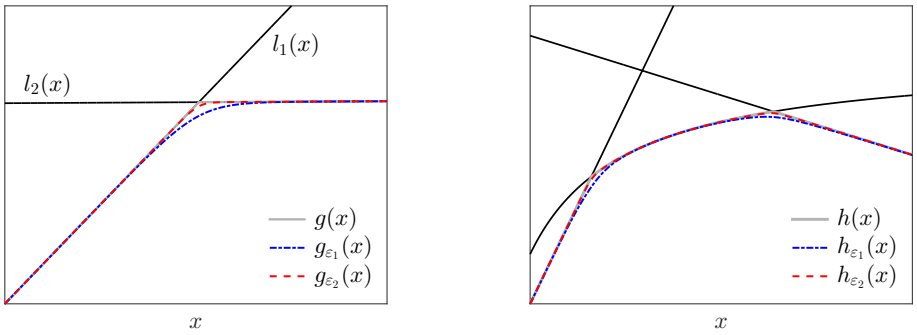

(a) (b)

Figure 5.4: Smooth approximation of two-segment piecewise linear functions defined in (5.2.6) and of the piecewise non-linear function defined in (5.2.12), for smoothing parameter values $\varepsilon_1 = 0.1$ and $\varepsilon_2 = 0.03$.

5.2.2.3 Numerical Parameter Estimation

Returning to our application, equations (5.2.4) and (5.2.5) suggest that the breakpoints ξ and ξ_2 in (5.2.6) and (5.2.12), respectively, correspond to the unknown flow parameter $v_m > 0$. For small $\varepsilon > 0$ we define the functions

$$\hat{g}_\varepsilon : \mathbb{R}^n \times \mathbb{R}^4 \to \mathbb{R}^n, \quad \hat{g}_\varepsilon(\hat{v}; \alpha, \beta, \gamma, \xi) = \alpha \mathbb{1} + \beta \hat{v} - \varepsilon \ln\left(\mathbb{1} + \mathrm{e}^{-\gamma(\hat{v} - \xi\mathbb{1})/\varepsilon}\right) \tag{5.2.18}$$

$$\hat{h}_\varepsilon : \mathbb{R}^n_+ \setminus \{0\} \times \mathbb{R}^5 \times \mathbb{R}_+ \setminus \{0\} \to \mathbb{R}^n, \tag{5.2.19}$$

$$\hat{h}_\varepsilon(\hat{v}; \alpha, \beta, \delta, \phi_1, \phi_2, \xi_2) = (\alpha - \delta/\xi_1 + \delta/\xi_2 - \phi_1\xi_1 - \phi_2\xi_2)\mathbb{1} + \tag{5.2.20}$$

$$(\beta + \phi_1 + \phi_2)\hat{v} + \varepsilon \ln \frac{\left(\mathbb{1} + \mathrm{e}^{-2\left(\frac{1}{\hat{v}} - \frac{1}{\xi_1}\mathbb{1}\right)/\varepsilon}\right)^{\delta} \left(\mathbb{1} + \mathrm{e}^{-2(\hat{v} - \xi_1\mathbb{1})/\varepsilon}\right)^{\phi_1}}{\left(\mathbb{1} + \mathrm{e}^{-2\left(\frac{1}{\hat{v}} - \frac{1}{\xi_2}\mathbb{1}\right)/\varepsilon}\right)^{\delta} \left(\mathbb{1} + \mathrm{e}^{-2(\hat{v} - \xi_2\mathbb{1})/\varepsilon}\right)^{-\phi_2}}, \tag{5.2.21}$$

where $\delta = \delta_1 = -\delta_2$ and $\xi_1 = 1$ is fixed. In both definitions, division, the logarithmic and exponential functions are applied component-wise. Using the non-monotone spectral projected gradient method, see Section 4.2.1, we numerically minimize the functions

$$f_g(\alpha, \beta, \gamma, \xi) = \frac{1}{2}\|\hat{g}_\varepsilon(\hat{v}; \alpha, \beta, \gamma, \xi) - \hat{s}(\hat{v})\|_2^2, \quad 0 \le \xi \le 1, \tag{5.2.22}$$

and

$$f_h(\alpha, \beta, \delta, \phi_1, \phi_2, \xi_2) = \frac{1}{2}\|\hat{h}_\varepsilon(\hat{v}; \alpha, \beta, \delta, \phi_1, \phi_2, \xi_2) - \hat{s}(\hat{v})\|_2^2, \quad \xi_2 \ge 1, \tag{5.2.23}$$

where $\hat{v} = (\hat{v}_1, \ldots, \hat{v}_n)^T \in \mathbb{R}^n$ and $\hat{s}(\hat{v}) \in \mathbb{R}^n$, with respect to all parameters. The functions $\hat{g}_\varepsilon$ and $\hat{h}_\varepsilon$ are smooth with respect to $\alpha, \beta, \gamma, \xi$ and $\alpha, \beta, \delta, \phi_1, \phi_2, \xi_2$, respectively, which implies smoothness of f_g and f_h. The constraints on variables ξ and ξ_2

express the model conditions on the breakpoints for each case specified in (5.2.4) and (5.2.5).

Thus, numerically computed optimal values for ξ and ξ_2 yield an estimate for the unknown maximal velocity v_m. We illustrate this approach in the next section by estimating v_m with the proposed method on synthetic and real data.

5.2.3 Experiments

We demonstrate the proposed method for estimating the maximal velocity v_m using both synthetic and plane wave ultrasound data. The synthetic images are generated in order to validate the method with respect to the known true value for v_m, and to show that the method copes well with a range of realistic particle patterns that frequently occur in practice. The considered textures include:

(a) uniform distribution of Dirac particles at low density,
(b) uniform distribution of Dirac particles at high density, and
(c) white noise.

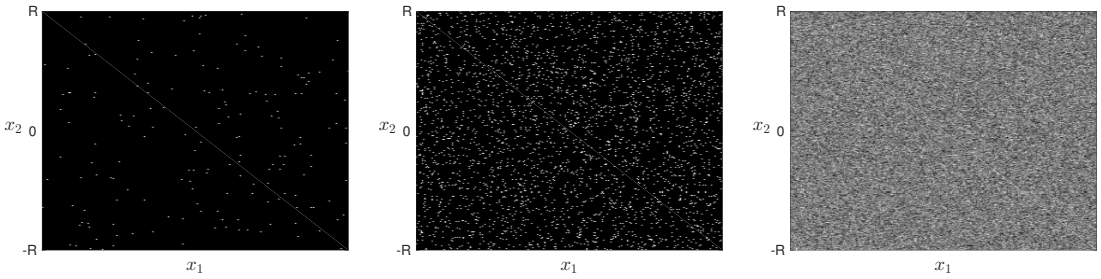

(a) (b) (c)

Figure 5.5: Synthetic textures of (a) uniformly distributed particles at low density, (b) uniformly distributed particles at high density and (c) uniform white noise. The flow is from left to right with periodic boundary conditions.

5.2.3.1 Ground Truth Data

Ground truth data consists of three synthetic textures, see Figure 5.5, driven by the Poiseuille flow model (2.2.1). For this, we choose two peak velocities $v_m = \{0.5, 5\}$ pixels/frame corresponding to the $v_m \leq 1$ and $v_m > 1$ case. We generated a discrete image sequence function $f(x,t)$ with 256 temporal frames of size 256×256 pixels. After computing the Fourier spectrum using Fast Fourier transform (FFT), see Figure 5.6, we numerically evaluated the integral (5.2.3) for a range of velocities $\{\hat{v}_n\}_n$. For the data set $\{(\hat{v}_n, \hat{s}(\hat{v}_n))\}_n$, we minimized the objective (5.2.22) or (5.2.23) and estimated the parameters of the smooth piecewise linear or non-linear functions which were fitted to the data. Figure 5.6, Table 5.1 and Table 5.2 summarize the obtained results.

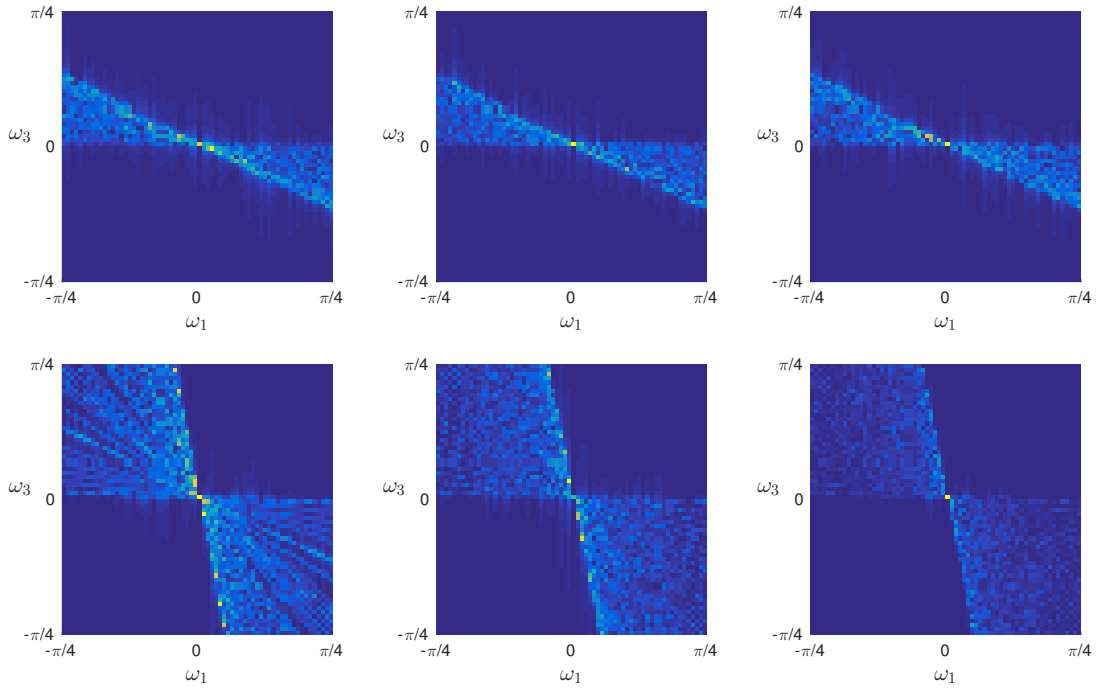

Figure 5.6: Fourier spectrum $|\hat{f}(\omega)|$ of the image sequence signal for each texture: (a) uniform distribution of particles at low density, (b) uniform distribution of particles at high density and (c) uniform white noise. TOP ROW: $v_m = 0.5$ pixels/frame. BOTTOM ROW: $v_m = 5$ pixels/frame. The images show a section of the spectral support in the plane $\omega_2 = 0$. The support of $|\hat{f}(\omega)|$ resembles the cone geometry illustrated in Figure 5.1.

	α	β	γ	$\xi = v_m$
Ground Truth	0	2.000	-2.000	0.500
(a) low density	-0.041	1.403	-1.390	0.713
(b) high density	-0.031	1.408	-1.402	0.703
(c) white noise	-0.028	1.418	-1.412	0.698

Table 5.1: Model parameters for piecewise linear function (5.2.4) and (5.2.6). Ground truth values are calculated from (5.2.11) for $v_m = 0.5$. By minimizing the objective function (5.2.22) we obtain the parameters of the smooth piecewise linear function (5.2.10b) that fits the data points $\{\hat{v}, \hat{s}(\hat{v})\}$ with the least squared error. The break-point ξ of this function coincides with the maximal flow velocity v_m that we wanted to determine.

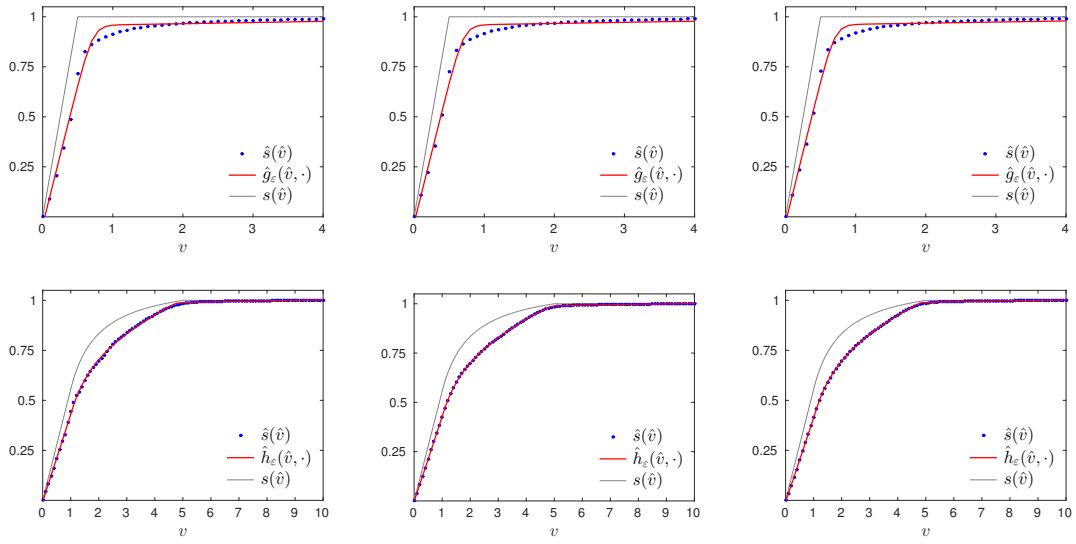

(a) (b) (c)

Figure 5.7: TOP ROW: Results for piecewise linear fitting for all considered textures driven by Poiseuille flow with maximal velocity $v_m = 0.5$ pixels/frame. BOTTOM ROW: Results for piecewise non-linear for $v_m = 5$ pixels/frame. The gray line marks the theoretical curve $s(v)$ predicted by (5.2.4) for $v_m = 0.5$ and (5.2.5) for $v_m = 5$, where $C_f = 1$. Blue dots denote the set $\{\hat{v}, \hat{s}(\hat{v})\}$, where $\hat{s}(\hat{v})$ was evaluated as a Riemannian sum which approximates the integral (5.2.3) with the Fourier spectrum $|\hat{f}(\omega)|$ estimated numerically for each texture, see Figure 5.6. The red solid line shows the smooth piecewise linear function (5.2.10b), with $\varepsilon = 0.1$ and parameters listed in Table 5.1, and the smooth piecewise non-linear function (5.2.15), with $\varepsilon = 0.03$ and parameters listed in Table 5.2, that minimizes (5.2.22) and (5.2.23), respectively.

	α	β	δ	ϕ_1	ϕ_2	$\xi_2 = v_m$
Ground Truth	0.500	0.273	0.273	-0.273	0	5.000
(a) low density	0.486	0.220	0.214	-0.189	-0.028	4.754
(b) high density	0.489	0.216	0.215	-0.187	-0.027	4.880
(c) white noise	0.487	0.211	0.230	-0.181	-0.028	4.797

Table 5.2: Model parameters for piecewise non-linear function (5.2.5) and (5.2.12). Ground truth values are calculated from (5.2.14) for $v_m = 5$. We estimated the parameters for each flowing texture by minimizing the objective function (5.2.23). According to (5.2.5), the breakpoint ξ_2 coincides with the maximal flow velocity v_m.

5.2.3.2 Ultrasound PIV: *In-Vitro* Data

We evaluated the proposed method on two sets of plane wave ultrasound images that image air-/micro-bubbles flow in a straight tube with different particle density, flow and frame rates. Table 5.3 summarizes all relevant imaging parameters. In Figure 5.8 we show one frame for both image sequences. Due to absorption of the acoustic wave the illumination of the tracer particles within the image is non-uniform.

The *in-vitro* experiment was performed under controlled conditions and the volume flow rate was measured with a flow-meter. This allows us to experimentally estimate the peak velocity using the equation

$$v_m = 2\frac{\Delta\Phi}{\pi R^2} \cdot \frac{N_x \Delta t}{L_x}, \tag{5.2.24}$$

that is valid for fully developed, laminar and steady pipe flows, where R is the radius of the tube and $\Delta\Phi$ is the volume flow rate. Here, the term $\frac{N_x \Delta t}{L_x}$ is used to convert the velocity units form m/s into pixels/frame. We refer to [VKV+16] for a more detailed description for this type of experiments.

As in the previous section, for each image sequence function $f(x,t)$ we compute the Fourier transform via FFT and the integral (5.2.3) as a Riemannian sum to obtain the set $\{(\hat{v}, \hat{s}(\hat{v}))\}$. Next, we fit a liner or non-linear piecewise smooth function to the data $\{(\hat{v}, \hat{s}(\hat{v}))\}$ by minimizing the appropriate objective function (5.2.22) or (5.2.23). We illustrate all intermediate steps in Figure 5.8 and summarize the final results in Table 5.4.

	Air-bubbles data	Microbubbles data
Tube radius R	0.005 m	0.005 m
Temporal frames	299	99
Image size $N_x \times N_z$	372×135	396×131
Frame rate	6.666 kHz	2.222 kHz
Temporal resolution Δt	0.150 ms	0.450 ms
Field of view size $L_x \times L_z$	3.8×1 cm^2	3.8×1 cm^2
Volume flow rate $\Delta\Phi$	15 ml/s	40 ml/s
Estimated v_m in m/s	0.382	1.019
Estimated v_m in px/frame	0.561	4.777

Table 5.3: Imaging parameters for air-/micro-bubbles data sets acquired in a plane wave ultrasound PIV experiment. In the last two rows we give the reference value for maximal flow velocity v_m calculated via equation (5.2.24).

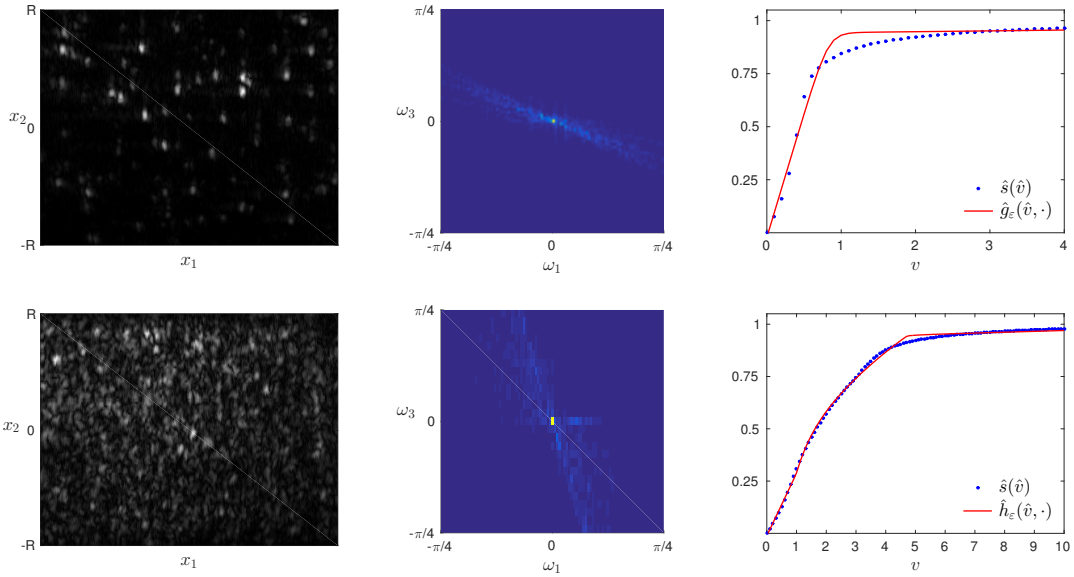

(a) (b) (c)

Figure 5.8: TOP ROW: Air-bubbles. BOTTOM ROW: Microbubbles. (a) An ultrasound frame. (b) Fourier spectrum $|\hat{f}(\omega)|$ of the image sequence signal in the plane $\omega_2 = 0$. (c) Results for the piecewise linear and non-linear fitting for air-bubbles and microbubbles data sets, respectively, with model parameters listed in Table 5.4.

	α	β	γ	$\xi = v_m$
Reference	0	1.783	-1.783	0.561
Air-bubbles flow	-0.022	1.166	-1.162	0.828

	α	β	δ	ϕ_1	ϕ_2	$\xi_2 = v_m$
Reference	0.500	0.279	0.279	-0.279	0	4.777
Microbubbles flow	0.459	0.152	0.203	-0.104	-0.044	4.723

Table 5.4: Model parameters for piecewise linear (5.2.4)/(5.2.6) and non-linear (5.2.5)/(5.2.12) functions evaluated by minimizing the objective function (5.2.22) and (5.2.23) for air-bubbles and microbubbles data sets, respectively. The reference values were calculated via (5.2.11) and (5.2.14) for v_m given by (5.2.24).

We remark, that in practice the discrete and finite image sequence function does not have a constant amplitude of the spectrum as assumed in equation (5.2.1). Rather we have $|\hat{f}(\omega)| \leq C_f$. This leads to a more complicated behavior of the support function $s(v)$. The difference between the numerical $\hat{s}(\hat{v})$ and a piecewise linear or non-linear function modeling $s(v)$ can be noticed in all plots of Figure 5.7. The model mismatch could be the source of the slight but systematic overestimation for small *subpixel* peak velocities observed for both synthetic and ultrasound data as observed in the numerical results in Tables 5.1 and 5.4.

5.3 Local Spatio-Temporal Approach

High temporal resolution of the signal acquired in plane wave ultrasound measurements leads to displacements that enable the application of differential motion estimation techniques. This motivates the use of a spatio-temporal filter bank approach for *local* motion extraction. The design of orientation- and motion-sensitive local filters has a long tradition in image processing and computer vision [Hee88, FJ90, Hag92], in models of early natural vision [AB85, MH08] and in the wavelet community [MK98]. Our goal is a proper discretization of a half-space in the spatio-temporal Fourier domain (which only is relevant for real-valued signals), in terms of a collection of motion-sensitive filters whose spectral support form a partition of unity to achive uniform motion sensitivity.

5.3.1 Spatio-Temporal Filter Bank

In this section, we detail the design of a spatio-temporal filter bank. The representation in spherical coordinates enables to illustrate the radial dependency in 1D and the two angular dependencies in 2D and 3D, respectively.
Design Criteria. The major aspects are:

- Self-similar parametrization in terms of a sequence of center frequencies, such that all filters form a partition of unity of the frequency interval $[\frac{\pi}{16}, \frac{\pi}{4}]$. The range originates from the following considerations: structures that generate lower frequencies are not relevant in our scenario, and the dependency on the global mean is removed. Frequencies larger than $\frac{\pi}{2}$ are regarded as noise.

- All filters form a partition of unity of both angular ranges. We thereby ignore an arbitrary half-space due to the symmetry of real signals in the Fourier domain.

The Log-Normal Filters. The transfer function of the one-dimensional log-normal filter with center frequency $\omega_i \geq 0$ and width $\sigma_i \geq 0$ is given by

$$\hat{g}_i(\omega) = \frac{1}{C(\sigma_i)} \frac{\omega_i}{\omega} \exp\left[-\frac{1}{2} \left(\frac{\log(\frac{\omega}{\omega_i})}{\sigma_i} \right)^2 \right], \quad \omega \geq 0, \tag{5.3.1}$$

where $C(\sigma_i) = \sqrt{2\pi}\sigma_i$. The norm of each filter is

$$\|\hat{g}_i\|_{L^1(\mathbb{R}_+)} = \omega_i. \tag{5.3.2}$$

The set of center frequencies and frequency widths

$$\omega_i = c^{(i-1)}\omega_1, \quad \sigma_i^2 = \log \frac{\omega_{i+1}}{\omega_i} = \log c, \qquad c > 1,\ i = 1, 2, \ldots \tag{5.3.3}$$

defines a filter bank $\{\hat{g}_i(\omega)\}_{i\geq 1}$ given by (5.3.1) such that $\hat{g}_{i+1}(\omega) = \frac{\omega}{\sqrt{\omega_i \omega_{i+1}}} \hat{g}_i(\omega)$. These parameters are also used below in the case of 2D and 3D filter banks.

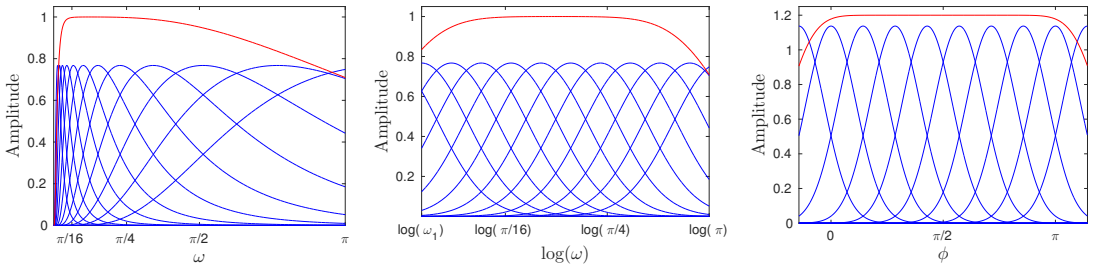

(a) (b) (c)

Figure 5.9: (a) The log-normal bandpass filter bank with $\omega_1 = \pi/50$ and $c = 1.5$ defining the parameter values (5.3.3). (b) Summing up the filter responses enables almost uniform detection of spectral signal support within the interval $\omega \in [\frac{\pi}{16}, \frac{\pi}{4}]$, cf. (5.3.4). (c) The angular part $\hat{g}_j(\phi)$ defined by (5.3.5) also provides a partition of unity within the interval $\phi \in [0, \pi]$.

Figure 5.9 illustrates this filter bank and also shows that it approximately provides a partition of unity of the frequency range of interest,

$$\sum_{i \in [12]} \hat{g}_i(\omega) \approx \text{constant}, \quad \text{for } \omega \in \left[\frac{\pi}{16}, \frac{\pi}{4}\right]. \tag{5.3.4}$$

In particular, very low frequencies and the global mean value of a signal, to which these filters are applied, are suppressed, as is the high-frequency range $\omega > \frac{\pi}{2}$ which is likely to be dominated by noise under realistic imaging conditions.

Extension to 2D. The extension of (5.3.1) to 2D reads

$$\hat{g}_{i,j}(\omega) = \frac{\omega_i}{\|\omega\|} \hat{g}_i(\|\omega\|) \hat{g}_j(\phi) = \tag{5.3.5}$$

$$= \frac{1}{C(\sigma_i)\, C(n_\phi)} \left(\frac{\omega_i}{\|\omega\|}\right)^2 \exp\left[-\frac{1}{2}\left(\frac{\log(\frac{\|\omega\|}{\omega_i})}{\sigma}\right)^2\right] \cos\left(\frac{\phi - \phi_j}{2}\right)^{2n_\phi}, \tag{5.3.6}$$

with polar coordinates $\omega = (\omega_1, \omega_2) \mapsto (\|\omega\|, \phi)$ on the right hand side and parameters: center frequency ω_i, frequency width σ, center angle ϕ_j, parameter $n_\phi \in \mathbb{N}$ and $C(n_\phi) = \frac{2\pi}{2^{2n_\phi}} \binom{2n_\phi}{n_\phi}$. In comparison to the one-dimensional case (5.3.1), this filter consists of a radial and an angular part. This *separability* is relevant for implementations of the filter in the spatial domain as convolution operators. The angular part yields orientation-selective filters whose selectivity can be tuned by selecting n_ϕ. In connection with the filter parameters (5.3.3), we fixed $n_\phi = 16$.

Figure 5.10 (c) illustrates the filters $\{\hat{g}_{i,j}(\omega)\}$ corresponding to the parameters (5.3.3), with additional center angles ϕ_j given by

$$\phi_j = (j-1)\frac{\pi}{7}, \qquad j \in \{0, 1, \ldots, 9\}. \tag{5.3.7}$$

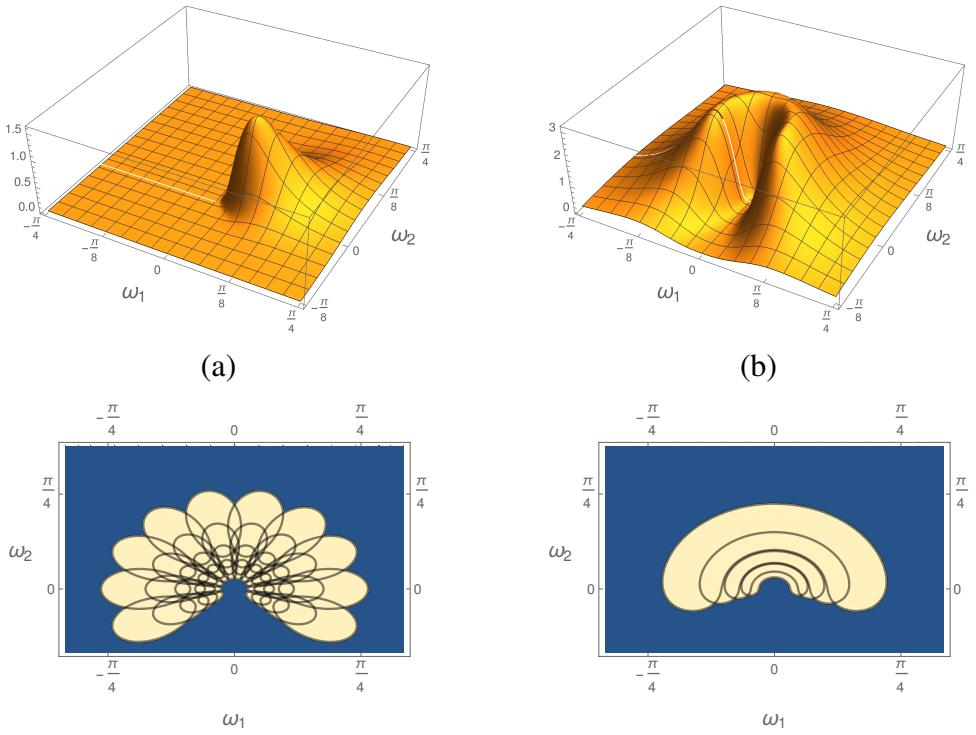

Figure 5.10: (a) Two dimensional log-normal filter defined by (5.3.5) for $i = 6$, $j = 2$. (b) The composed log-normal filter $G_i(\omega)$ given by (5.3.11) illustrates the contribution of all filters at a single center frequency to the entire angular range. (c) Contours of log-normal filters illustrate the self-similar design and the partition of unity. (d) Contours of the composed log-normal filters used as a filter bank for our application.

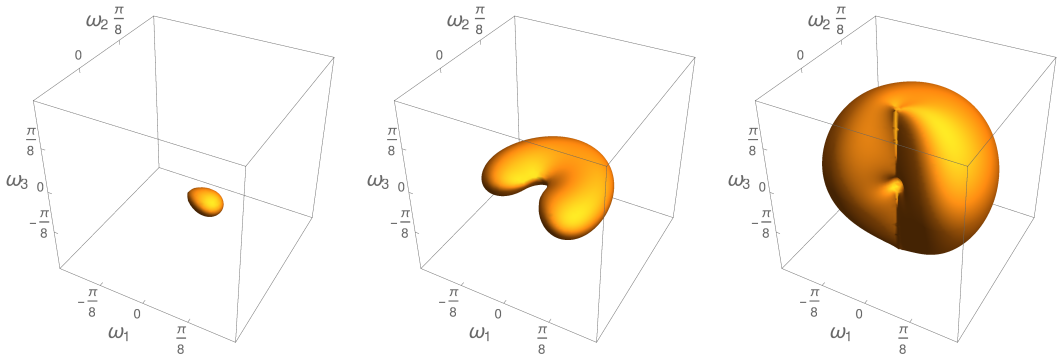

(a) (b) (c)

Figure 5.11: (a) Illustration of the extensions of the 2D filter to 3D defined by (5.3.8) for parameters $i = 7$, $j = 1$, $k = 5$. (b) $\sum_j \hat{g}_{i,j,k}(\omega)$ for fixed $i = 7$ and $k = 5$. (c) $G_i(\omega) = \sum_{j,k} \hat{g}_{i,j,k}(\omega)$ for fixed $i = 7$ (cf. (5.3.11)).

Extension to 3D. In spherical coordinates $\omega = (\omega_1, \omega_2, \omega_3) \mapsto (\|\omega\|, \theta, \phi)$, our three-dimensional version of the log-normal filter reads

$$\hat{g}_{i,j,k}(\omega) = \left(\frac{\omega_i}{\|\omega\|}\right)^2 \hat{g}_i(\|\omega\|)\hat{g}_j(\phi)\hat{g}_k(\theta) = \tag{5.3.8}$$

$$\frac{1}{C}\left(\frac{\omega_i}{\|\omega\|}\right)^3 \exp\left[-\frac{1}{2}\left(\frac{\log(\frac{\|\omega\|}{\omega_i})}{\sigma}\right)^2\right] \cos\left(\frac{\phi-\phi_j}{2}\right)^{2n_\phi} \cos\left(\frac{\theta-\theta_k}{2}\right)^{2n_\theta}, \tag{5.3.9}$$

with the normalizing factor $C = C(\sigma)C(n_\phi)C(n_\theta)$, $C(n_\phi) = C(n_\theta)$ and $n_\phi = n_\theta$. The center values of the additional angular variable are

$$\theta_k = (k-1)\frac{\pi}{7}, \quad k \in [8]. \tag{5.3.10}$$

Figure 5.11 illustrates the resulting filters. The proposed filter bank is designed to be sensible to flow in all directions and independent of the orientation angle. For this reason we sum up several filters along the angular parameters and consider the remaining radial component ω_i as the only filter parameter.

Spatio-Temporal Filter Bank. The filter bank is parametrized by the finite set of center frequency values ω_i and defined by

$$\hat{G}_i(\omega) = \sum_j \hat{g}_{i,j}(\omega) \quad \textbf{(in 2D)} \quad \text{and} \quad \hat{G}_i(\omega) = \sum_{j,k} \hat{g}_{i,j,k}(\omega), \quad \textbf{(in 3D)} \tag{5.3.11}$$

where $\hat{g}_{i,j}(\omega)$ and $\hat{g}_{i,j,k}(\omega)$ are given by (5.3.5) and (5.3.8), respectively. The parameters are listed in (5.3.3), (5.3.7), (5.3.10).

5.3.2 Local Velocity Estimation

For an image sequence $f(x,t)$, the response function of a filter G_i (5.3.11) reads

$$h_i(x,t) = (f * G_i)(x,t) = \mathcal{F}^{-1}(\hat{f} \cdot \hat{G}_i)(x,t) = r_i(x,t)e^{\mathbf{i}\psi_i(x,t)}, \tag{5.3.12}$$

with the amplitude function $r_i(x,t) = |h_i(x,t)|$ and the phase function

$$\psi_i(x,t) = \arg(h_i(x,t)) = \Im(\ln(h_i(x,t))) \in (-\pi,\pi]. \tag{5.3.13}$$

The basic assumption underlying local motion estimation is that *phase functions* $\psi_i(x,t)$ *are approximately conserved under motion*, that is

$$\frac{\mathrm{d}}{\mathrm{d}t}\psi_i = \langle \nabla\psi_i(x,t), (\dot{x},1)\rangle = \langle \nabla_x\psi_i(x,t), \dot{x}\rangle + \partial_t\psi_i(x,t) \approx 0, \quad \forall (x,t). \tag{5.3.14}$$

As a result, after estimating the partial derivatives of all functions ψ_i, we estimate the velocity $v = \dot{x}$ *for any fixed space-time point* (x,t) by minimizing the squared residual error of the latter equation, namely

$$u(x,t) = \arg\min_v \sum_i \left(\langle \nabla_x\psi_i(x,t), v\rangle + \partial_t\psi_i(x,t)\right)^2. \tag{5.3.15}$$

Estimating the partial derivatives of $\psi(x,t)$. We express the partial derivatives $\nabla\psi$ by partial derivatives of a *smooth* signal h, as follows

$$h = re^{\mathbf{i}\psi}, \qquad \nabla h = (\nabla r)e^{\mathbf{i}\psi} + (re^{\mathbf{i}\psi})(\mathbf{i}\nabla\psi) = e^{\mathbf{i}\psi}\nabla r + \mathbf{i}h\nabla\psi \tag{5.3.16a}$$

$$\nabla\psi = \frac{1}{|h|^2}\Im(\overline{h}\nabla h), \qquad \overline{h}\nabla h = re^{-\mathbf{i}\psi}\nabla h = r\nabla r + \mathbf{i}|h|^2\nabla\psi. \tag{5.3.16b}$$

We numerically estimate the partial derivatives of ∇h by separable 3D filters whose frequency response are obtained by an orthogonal expansion of the desired behaviour in the Fourier domain (derivative filter at low frequencies, noise suppression at high frequencies) using Krawtchouk polynomials [HS87, YPO03]. These filters are similar to derivative-of-Gaussian filters but avoid aliasing artefacts in the case of filters with small spatial support, that would result from merely sampling the continuous impulse response.

5.3.3 Experiments

In Section 5.3.3.1 we report synthetic experiments for 1D image sequences that validate and illustrate the filter bank design, followed by 2D pipe flow scenarios in Sections 5.3.3.2 and 5.3.3.3, including real *in-vitro* data in laminar and turbulent flow scenarios.

5.3.3.1 One-Dimensional Synthetic Sequences with Ground Truth

We illustrate the filter characteristics for the following 1D scenarios:

(a) Harmonic oscillation of a single particle, $x(t) = a\sin(\omega t)$, where $a > 0$ is the amplitude and $\omega > 0$ is the angular frequency.
(b) Elastic collision of two point particles moving with constant velocity.
(c) Flow of multiple particles with velocities

$$\dot{x} = v(x) = \begin{cases} -\alpha x^2, & x \leq 0 \\ \alpha x^2, & x > 0 \end{cases}, \qquad \alpha > 0. \tag{5.3.17}$$

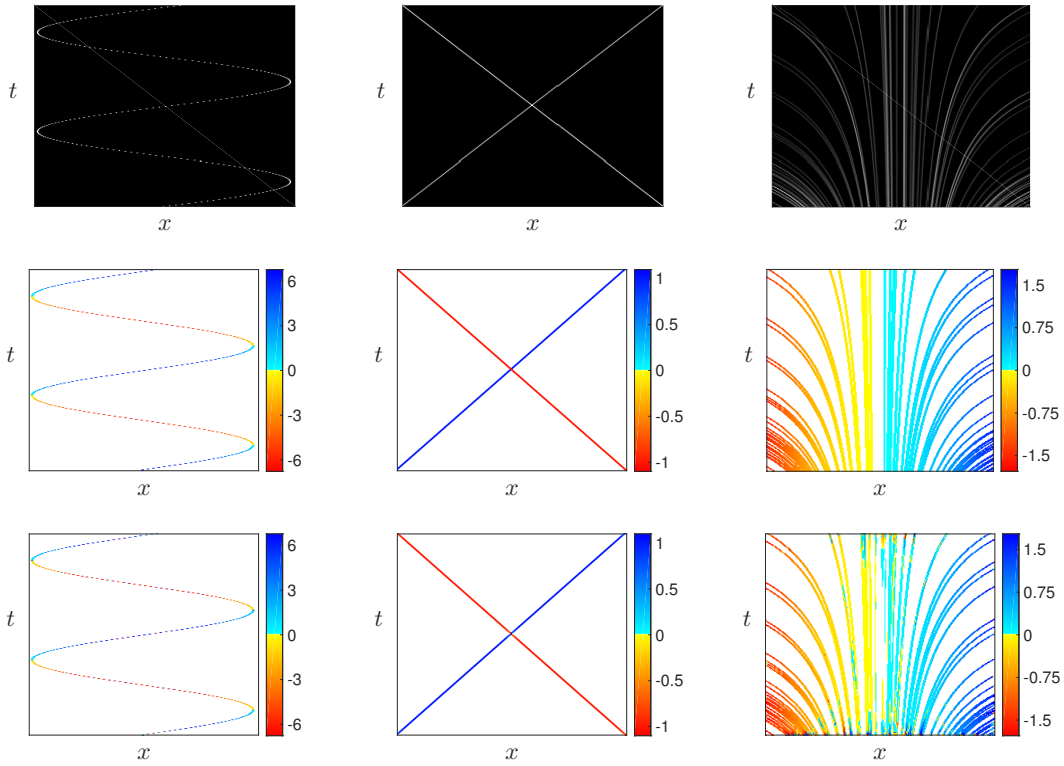

Figure 5.12: TOP ROW: Space-time trajectories for the 1D image sequences of Section 5.3.3.1. CENTER ROW: Ground truth velocities with velocity magnitude depicted in the colormap. BOTTOM ROW: Estimated velocities for the harmonic oscillator (a), the elastic collision of two particles (b) and for the flow of multiple particles (c), using the phase functions displayed by Figure 5.13. These estimates are accurate except for small regions close to the boundaries in trajectory direction, that exhibit natural errors caused by overlapping filter supports.

Figure 5.12 illustrate the image sequences in terms of space-time trajectories of the particles and their velocities. Figure 5.13 illustrate the phase functions of the aggregated complex filter responses (5.3.11). Due to the smoothness of these functions, velocity estimates are accurate even though moving particles cause sharp intensity changes in the spatio-temporal domain.

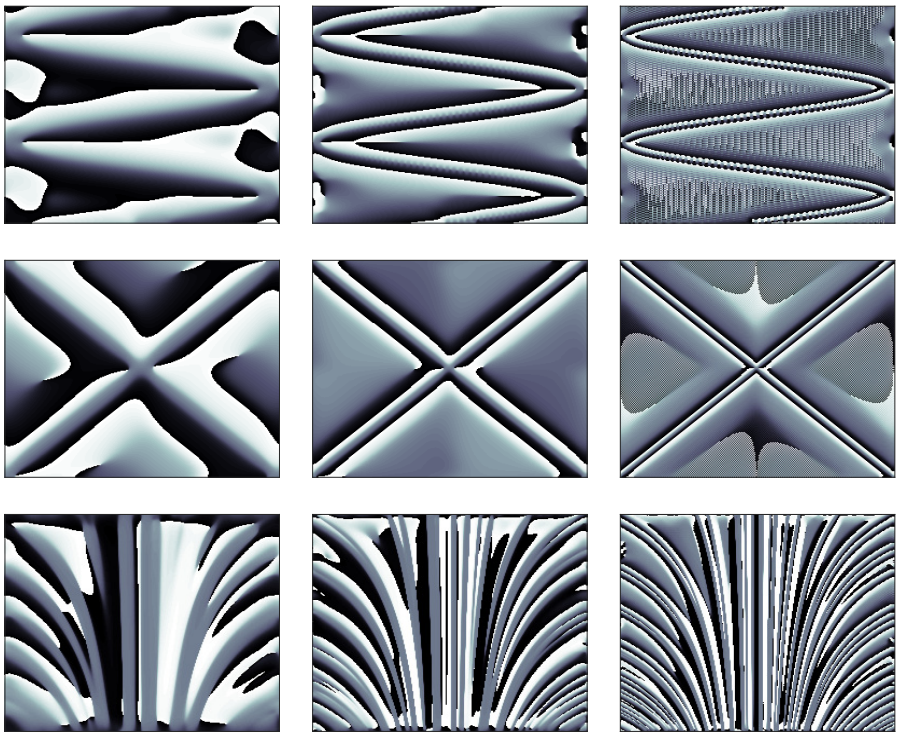

(a) (b) (c)

Figure 5.13: COLUMNS: Phase output ψ_i due to (5.3.13) for center frequencies ω_i given by (5.3.3) and $i \in \{5, 7, 9\}$. ROWS: The 1D image sequences of Section 5.3.3.1. These plots illustrate that even for the 1D sequences with low particle density, combining multiple filter responses due to (5.3.11) enables to *locally* estimate motion information at every spatio-temporal point (x, t).

5.3.3.2 Laminar Pipe Flow: Ground Truth Data

We validated the proposed method in 2D using synthetic image sequences of uniformly distributed point-particles, driven by laminar pipe flow in (2.2.1). We generated a spatial-temporal dataset of size $256 \times 256 \times 256$ with peak velocities in the range $v_m \in \{0.5, 1, ..., 4, 4.5\}$ pixels/frame. We estimated the velocity field by minimizing (5.3.15) using the 3D filter bank in (5.3.11). The results are shown in Figure 5.14.

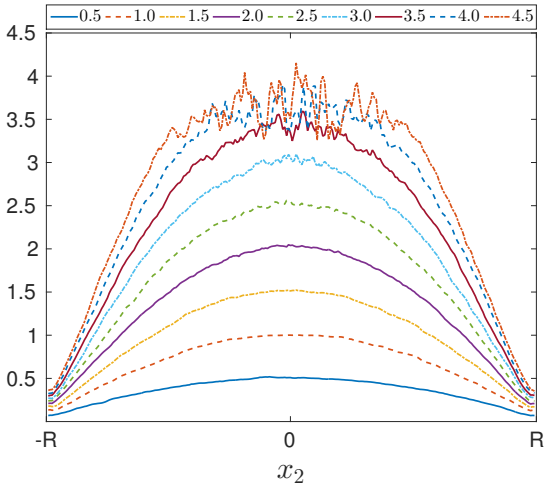

Figure 5.14: Estimates of time-averaged velocity profiles for several peak velocities v_m. The parabolic profile is well reconstructed if $v_m < 3$. For $v_m \geq 3$, motion-induced temporal frequencies cause aliasing effects (cf. [BPS15, Section 2.2.3]) at the center of the tube, which could be fixed by spatial subsampling.

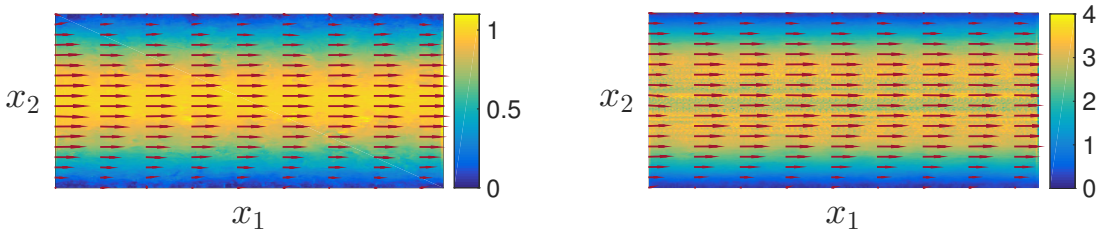

(a) (b)

Figure 5.15: Estimated time-averaged velocity fields for maximal velocity (a) $v_m = 1$ pixels/frame and (b) $v_m = 4$ pixels/frame with velocity magnitude depicted in the colormap. The local approach can not estimate large particle displacements due to the high velocities in the center of the tube as observed in Figure 5.14.

5.3.3.3 Ultrasound PIV: *In-Vitro* Data

Figure 5.16 depicts real *in-vitro* flows for both a *laminar* and a *turbulent* scenario, along with time-averaged local flow estimates $\hat{u}(x^{(k)}) = \left(\hat{u}_1(x^{(k)}), \hat{u}_2(x^{(k)})\right)^\top$ based on (5.3.15) and parameter estimates v_m and N of the flow model (2.2.2). The *in-vitro* Echo PIV experiments imaging the flow in a pipe of a fluid seeded with air bubbles were performed under controlled conditions. The relevant experimental parameters include: image acquisition rate $f = 6.66$ kHz, fluid density $\rho = 1038$ kg/m^3, viscosity $\mu = 4.1$ mPa·s, radius of the pipe $R = 5$ mm, field of view 21.3×37.8 mm^2, image size 288×384 and number of temporal frames 298.

	Q [m^3/s]	Re	v_m	N	$v_{(ave)}$	$v^*_{(ave)}$
laminar flow	$15 \cdot 10^{-6}$	484	0.356	1.361	0.193	0.295
turbulent flow	$80 \cdot 10^{-6}$	2579	1.557	3.547	1.081	1.577

Table 5.5: ***In-vitro* ultrasound experiments.** Relevant parameters: volume flow rate Q, measured with a flow-meter, and Reynolds number Re. Estimated parameters (cf. (2.2.2)): v_m, N; relation to the average velocity $v_{(ave)} = v_m(N+1)/(N+3)$; independent reference value for the average velocity: $v^*_{(ave)} = Q/(\pi R^2)$. The velocities are given in pixels/frame.

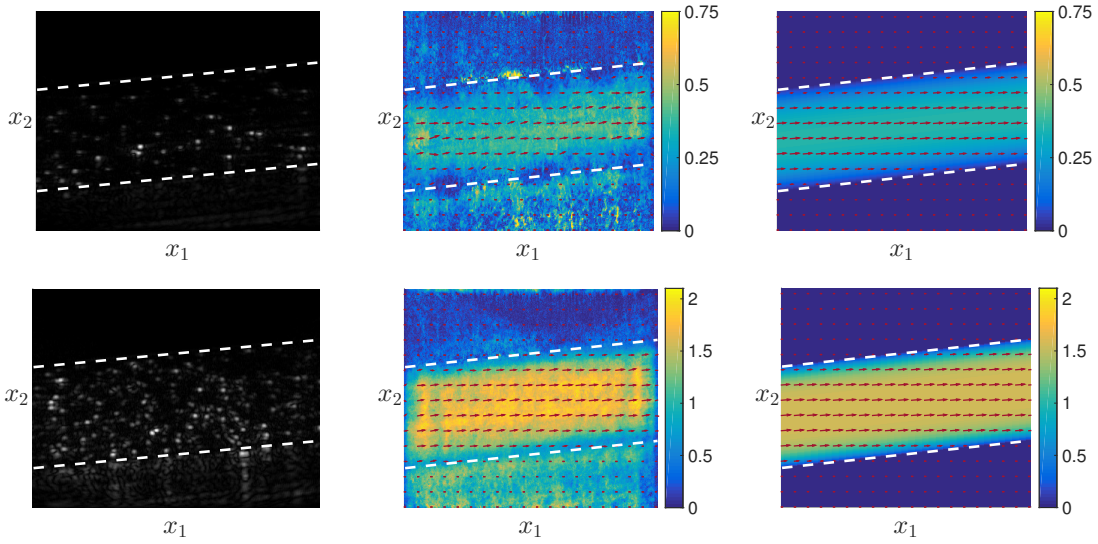

Figure 5.16: ***In-vitro* data.** TOP ROW: laminar steady flow. BOTTOM ROW: turbulent flow. (a) An image of the tracer particles, (b) time-averaged local velocity field estimate and (c) flow model estimate with velocity magnitude depicted in the colormap. Table 5.5 reports quantitative results.

We obtain parameter estimates v_m and N by minimizing the objective

$$f(v_m, N) = \sum_k \left\| \hat{u}(x^{(k)}) - R(\vartheta) u(x^{(k)}; v_m, N) \right\|^2, \quad v_m \geq 0,\ N \geq 1, \tag{5.3.18}$$

where the rotation matrix $R(\vartheta)$ accounts for the tilted pipe (indicated by the dashed lines in Figure 5.16) and $u(x^{(k)}; v_m, N)$ is given by (2.2.2). The sum runs over all image points $x^{(k)}$ contained in the interior of the tube. The minimization problem was solved using the spectral projected gradient method, see Section 4.2.1, using the default parameters specified in [BMR00] and with the non-monotone parameter value $M = 2$. The initial values for v_m and N where randomly chosen in the intervals $(0, 2)$ and $(1, 4)$, respectively. The program was stopped after 10 iterations. The estimated

velocity fields depicted by Figure 5.16 and the quantitative results in Table 5.5 show that our method achieves realistic estimates. The reference value $v^*_{(ave)}$ is calculated from the volume flow rate Q that was measured during the experiment.

Chapter 6

Conclusion

In this thesis we investigated the problem of image reconstruction and motion estimation related to plane wave ultrasound particle image velocimetry.

In Chapter 3 we considered a simplified model of wave propagation in uniform medium, which neglects multiple scattering in view of the Born approximation, the shape of the incident wave and the decay factor in the amplitude of the travel waves, in order to formulate an image reconstruction approach that scales well with the size of the problems encountered in realistic applications such as plane wave ultrasound imaging. We discussed the Delay and Sum reconstruction method and its relation to the solution of the inverse problems via least squares minimization. Numerical evaluations showed that Delay and Sum and least squares minimization methods visually produce similar results.

In Chapter 4 we reformulated the velocity estimation problem in Echo PIV for laminar and steady flows as a parametric sparse reconstruction problem. We defined a sparsifying dictionary consisting of space-time trajectories of individual particles, which is updated during the iterative process and robustly refines the unknown velocity information. We analyzed and tested the several minimization schemes on synthetic and real *in-vitro* data. The generalization of the trajectory dictionary to multiple-flow parameter models, e.g. the pulsatile blood flows [Wom55] remains as future work.

In the first part of Chapter 5, we presented a global method for estimating the maximum velocity for pipe flows based on the cone geometry of the spectral support in the Fourier domain of the image sequence function. In the second part, we proposed a variational method for extracting the local velocity field information based on a carefully design spatio-temporal filter bank that is sensitive to all flow directions.

The proposed motion estimation approaches have several attractive features. First, they work directly on given image sequence data without the need for any image preprocessing. Second, since they are global methods it is expected to cope better with noisy scenarios that are encountered in real applications. Finally, the numerical computations are simple enough to make conceivable real-time implementations.

Bibliography

[AARW17] G. S. Alberti, H. Ammari, F. Romero, and T. Wintz. Mathematical analysis of ultrafast ultrasound imaging. *SIAM Journal on Applied Mathematics*, 77(1):1–25, 2017.

[AB85] E. H. Adelson and J. R. Bergen. Spatiotemporal Energy Models for the Perception of Motion. *Journal of the Optical Society of America A*, 2(2):284–299, 1985.

[Adr11] J. Adrian, R.J.and Westerweel. *Particle Image Velocimetry*. Cambridge University Press, 2011.

[AGJ+13] H. Ammari, J. Garnier, W. Jing, H. Kang, M. Lim, K. Solna, and H. Wang. *Mathematical and Statistical Methods for Multistatic Imaging*. Springer, 2013.

[AGK+11] H. Ammari, J. Garnier, H. Kang, W.-K. Park, and K. Sølna. Imaging schemes for perfectly conducting cracks. *SIAM Journal on Applied Mathematics*, 71(1):68–91, 2011.

[BCS01] N. Bleistein, J. K. Cohen, and J. W. Jr. Stockwell. *Mathematics of Multidimensional Seismic Imaging, Migration, and Inversion*. Springer, 2001.

[BGPS15] E. Bodnariuc, A. Gurung, S. Petra, and C. Schnörr. Adaptive Dictionary-Based Spatio-temporal Flow Estimation for Echo PIV. In *Proc. EMMCVPR*, volume 8932 of *LNCS*, pages 378–391. Springer, 2015.

[BGPT01] L. Borcea, J. Garnier, G. Papanicolaou, and C. Tsogka. Coherent interferometric imaging, time gating and beamforming. *Inverse Problems*, 27:1–17, 201.

[BMR00] E. G. Birgin, J. M. Martinez, and M. Raydan. Nonmonotone Spectral Projected Gradient Methods on Convex Sets. *SIAM Journal on Optimization*, 10(4):1196–1211, 2000.

[Bod18] E. Bodnariuc. A Spectral Approach to Peak Velocity Estimation of Pipe Flows from Noisy Image Sequences. *Analele Stiintifice ale Univesitatii Ovidius Constanta*, 2018. (accepted).

[Bor15] L. Borcea. Imaging in random media. In O. Scherzer, editor, *Handbook of Mathematical Methods in Imaging*, pages 1279 – 1340. Springer, 2015.

[BPPS16] E. Bodnariuc, S. Petra, C. Poelma, and C. Schnörr. Parametric Dictionary-Based Velocimetry for Echo PIV. In *GCPR*, volume 9796 of *Lecture Notes in Computer Science*, pages 332–343. Springer, 2016.

[BPS15] F. Becker, S. Petra, and C. Schnörr. Optical Flow. In O. Scherzer, editor, *Handbook of Mathematical Methods in Imaging*, pages 1945–2004. Springer, 2nd edition, 2015.

[BPSV17] E. Bodnariuc, S. Petra, C. Schnörr, and J. Voorneveld. A Local Spatio-Temporal Approach to Plane Wave Ultrasound Particle Image Velocimetry. In *GCPR*, volume 10496 of *Lecture Notes in Computer Science*, pages 138–149, 2017.

[BS00] J. F. Bonnans and A. Shapiro. *Perturbation Analysis of Optimization Problems*. Springer, 2000.

[BSPS16] E. Bodnariuc, M. Schiffner, S. Petra, and C. Schnörr. Plane Wave Acoustic Superposition for Fast Ultrasound Imaging. In *International Ultrasonics Symposium (IUS)*. IEEE, 2016.

[BT09] A. Beck and M. Teboulle. A Fast Iterative Shrinkage-Thresholding Algorithm for Linear Inverse Problems. *SIAM Journal on Imaging Sciences*, 2(1):183–202, 2009.

[BZV+16] A. Besson, M. Zhang, F. Varray, H. Liebgott, D. Friboulet, Y. Wiaux, J.-P. Thiran, R. E. Carrillo, and O. Bernard. A Sparse Reconstruction Framework for Fourier-Based Plane-Wave Imaging. *IEEE Ultrasonics, Ferroelectrics, and Frequency Control*, 63(12):2092–2106, 2016.

[CCM00] D. Colton, J. Coyle, and P. Monk. Recent Developments in Inverse Acoustic Scattering Theory. *SIAM Review*, 42:369–414, 2000.

[CE14] T. Chernyakova and Y. C. Eldar. Fourier-domain beamforming: the path to compressed ultrasound imaging. *IEEE Transactions on Ultrasonics, Ferroelectrics and Frequency Control*, 61(8), 2014.

[CFT12] O. Couture, M. Fink, and M. Tanter. Ultrasound contrast plane wave imaging. *IEEE Transactions on Ultrasonics, Ferroelectrics and Frequency Control*, 59(12), 2012.

[CGT00] A. R. Conn, N. I. M. Gould, and P. L. Toint. *Trust Region Methods*. MPS-SIAM, 2000.

[CK13] D. Colton and R. Kress. *Inverse Acoustic and Electromagnetic Scattering Theory*. Springer, 3rd edition, 2013.

[CMP13] A. Chai, M. Moscoso, and G. Papanicolaou. Robust imaging of localized scatterers using the singular value decomposition and ℓ_1 minimization. *Inverse Problems*, 29(2), 2013.

[CMP14] A. Chai, M. Moscoso, and G. Papanicolaou. Imaging strong localized scatterers with sparsity promoting optimization. *SIAM Journal on Imaging Sciences*, 7(2):1358–1387, 2014.

[CPTP16] M. Correia, J. Provost, M. Tanter, and M. Pernot. 4D Ultrafast Ultrasound Flow Imaging In Vivo Quantification of Arterial Volumetric Flow Rate in a Single Heartbeat. *Physics in Medicine & Biology*, 61(23):L48–L61, 2016.

[DDP+15] C. Demene, T. Deffieux, B.-F. Pernot, M.and Osmanski, V. Biran, J.-L. Gennisson, L.-A. Sieu, A. Bergel, S. Franqui, J.-M. Correas, I. Cohen, O. Baud, and M. Tanter. Spatiotemporal Clutter Filtering of Ultrafast Ultrasound Data Highly Increases Doppler and fUltrasound Sensitivity. *IEEE Transactions on Medical Imaging*, 34(11), 2015.

[DG10] N. Dominguez and V. Gibiat. Non-destructive imaging using the time domain topological energy method. *Ultrasonics*, 50(3):367–372, 2010.

[DRZL15] G. David, J. L. Robert, B. Zhang, and A. F. Laine. Time domain compressive beam forming of ultrasound signals. *Journal of the Acoustical Society of America*, 137(5), 2015.

[Eva10] L. C. Evans. *Partial Differential Equations*. American Mathematical Society, 2010.

[FJ90] D. J. Fleet and A. D. Jepson. Computation of Component Image Velocity from Local Phase Information. *International Journal of Computer Vision*, 5(1), 1990.

[Fol45] L. L. Foldy. The multiyle scattering of waves. i. general theory of isotroyic scattering by randomly distributed scatterers. *Physical Review*, 67(3-4):107–119, 1945.

[FR13] S. Foucart and H. Rauhut. *A Mathematical Introduction to Compressive Sensing*. Birkhäuser Basel, 2013.

[Geo15] S. G. Georgiev. *Theory of Distributions*. Springer, 2015.

[GTM+13] D. Garcia, L. L. Tarnec, S. Muth, E. Montagnon, J. Poree, and G. Cloutier. Stolt's f-k migration for plane wave ultrasound imaging. *IEEE Transactions on Ultrasonics, Ferroelectrics, and Frequency Control*, 60(9):1853–1867, 2013.

[Had23] J. Hadamard. *Lectures on Cauchy's Problem in Linear Partial Differential Equations*. Yale University Press, New Haven, 1923.

[Hag92] L. Haglund. *Adaptive Multidimensional Filtering*. PhD thesis, Dept. Electrical Engineering, University of Linköping, Sweden, 1992.

[Hee88] H. J. Heeger. Optical flow using spatiotemporal filters. *International Journal of Computer Vision*, 1(4), 1988.

[HPT+08] G.-R. Hong, G. Pedrizzetti, G. Tonti, P. Li, Z. Wei, J. K. Kim, A. Baweja, S. Liu, N. Chung, H. Houle, J. Narula, and M. A. Vannan. Characterization and Quantification of Vortex Flow in the Human Left Ventricle by Contrast Echocardiography Using Vector Particle Image Velocimetry. *JACC: Cardiovascular Imaging*, 1(6):705–717, 2008.

[HS87] M. Hashimoto and J. Sklansky. Multiple-Order Derivatives for Detecting Local Image Characteristics. *Computer Vision, Graphics, and Image Understanding*, 39:28–55, 1987.

[Jen96] J. A. Jensen. Field: A program for simulating ultrasound systems. In *10th Nordic-Baltic Conference on Biomedical Imaging Published in Medical & Biological Engineering & Computing*, volume 34, pages 351–353, 1996.

[JS92] J. A. Jensen and N. B. Svendsen. Calculation of pressure fields from arbitrarily shaped, apodized, and excited ultrasound transducers. *IEEE Transactions on Ultrasonics, Ferroelectrics, and Frequency Control*, 39:262–267, 1992.

[KHS04] H. Kim, J. Hertzberg, and R. Shandas. Development and Validation of Echo PIV. *Experiments in Fluids*, 36(3):455–462, 2004.

[Kir11] A. Kirsch. *An Introduction to the Mathematical Theory of Inverse Problems*. Springer, 2011.

[Kre10] R. Kress. *Linear Integral Equations*. Springer, 3rd edition, 2010.

[Lax51] M. Lax. Multiple scattering of waves. *Reviews of Modern Physics*, 23(4):287–310, 1951.

[LBE+15] C. H. Leow, E. Bazigou, R. J. Eckersley, A. C. H. Yu, P. D. Weinberg, and M. X. Tang. Flow Velocity Mapping Using Contrast Enhanced High-Frame-Rate Plane Wave Ultrasound and Image Tracking: Methods and Initial in Vitro and in Vivo Evaluation. *Ultrasound in Medicine and Biology*, 41(11), 2015.

[LRMC+16] H. Liebgott, A. Rodriguez-Molares, F. Cervenansky, J. A. Jensen, and O. Bernard. Plane-Wave Imaging Challenge in Medical Ultrasound. In *IEEE International Ultrasonics Symposium*. IEEE, 2016.

[MH08] C. Massot and J. Hérault. Model of Frequency Analysis in the Visual Cortex and the Shape from Texture Problem. *International Journal of Computer Vision*, 76:165–182, 2008.

[Min89] M. Minoux. *Mathematical Programming. Theory and Algorithms*. John Wiley and Sons, 1989.

[MK98] J. Margarey and N. Kingsbury. Motion Estimation Using a Complex-Valued Wavelet Transform. *IEEE Transactions on Signal Processing*, 46(4):1069–1084, 1998.

[MS93] R. Mifflin and J. J. Strodiot. A rapidly convergent five-point algorithm for univariate minimization. *Mathematical Programming*, 62:299–319, 1993.

[MTB+09] G. Montaldo, M. Tanter, J. Bercoff, N. Benech, and M. Fink. Coherent Plane-Wave Compounding for Very High Frame Rate Ultrasonography and Transient Elastography. *IEEE Transactions on Ultrasonics, Ferroelectrics and Frequency Control*, 56(3), 2009.

[Nat15] F. Natterer. Sonic imaging. In O. Scherzer, editor, *Handbook of Mathematical Methods in Imaging*, pages 1253–1278. Springer, 2015.

[Pie89] A. D. Pierce. *Acoustics: An Introduction to Its Physical Principles and Applications*. American Institute of Physics, 1989.

[Poe17] C. Poelma. Ultrasound Imaging Velocimetry: A Review. *Experiments in Fluids*, 58(1):3, 2017.

[PPA+14] J. Provost, C. Papadacci, J. E. Arango, M. Imbault, M. Fink, J.-L. Gennisson, M. Tanter, and M. Pernot. 3D ultrafast ultrasound imaging in vivo. *Physics in Medicine & Biology*, 2014.

[PvdMM+12] C. Poelma, R. M. E. van der Mijle, J. M. Mari, M. X. Tang, P. D. Weinberg, and J. Westerweel. Ultrasound Imaging Velocimetry: Toward Reliable Wall Shear Stress Measurements. *European Journal of Mechanics - B/Fluids*, 35:70–75, 2012.

[RJG13] S. Rodriguez, X. Jacob, and V. Gibiat. Plane wave echo particle image velocimetry. In *Proceeding of Meeting of Acoustic*, volume 19 of *Proceeding of Meeting of Acoustic*. Acoustical Society of America (ASA), 2013.

[RSGJ12] S. Rodriguez, P. Sahuguet, V. Gibiat, and X. Jacob. Fast topological imaging. *Ultrasonics*, 52(8):1010–1018, 2012.

[RW09] R.T. Rockafellar and R. J.-B. Wets. *Variational Analysis*. Springer, 2nd edition, 2009.

[RWWK07] M. Raffel, C. E. Willert, S. T. Wereley, and J. Kompenhans. *Particle Image Velocimery – A Practical Guide*. Springer, 2007.

[SCT+99] L. Sandrin, S. Catheline, M. Tanter, X. Hennequin, and M. Fink. Time-resolved pulsed elastography with ultrafast ultrasonic imaging. *Ultrasonic Imaging*, 1999.

[Shu15] K. K. Shung. *Diagnostic Ultrasound: Imaging and Blood Flow Measurements*. CRC Press. Taylor & Francis Group, 2015.

[SS12] M. F. Schiffner and G. Schmitz. Fast image acquisition in pulse-echo ultrasound imaging using compressed sensing. *IEEE International Ultrasonics Symposium (IUS)*, 2012.

[Sti14] J. Stigler. Analytical Velocity Profile in Tube for Laminar and Turbulent Flow. *Engineering Mechanics*, 21(6):371–379, 2014.

[Sza04] T. L. Szabo. *Diagnostic Ultrasound Imaging: Inside Out*. Elsevier Academit Press, 2004.

[TBSF02] M. Tanter, J. Bercoff, L. Sandrin, and M. Fink. Ultrafast compound and imaging for 2-d and motion and vector estimation : Application to transient elastography. *IEEE Ultrasonics, Ferroelectrics, and Frequency Control*, 2002.

[TF14] M. Tanter and M. Fink. Ultrafast Imaging in Biomedical Ultrasound. *IEEE Transactions on Ultrasonics, Ferroelectrics, and Frequency Control*, 61(1), 2014.

[VKV+16] J. Voorneveld, P. Kruizinga, H. J. Vos, F. J. H. Gijsen, E. G. Jebbink, A. F. W. van der Steen, N. de Jong, and J. G. Bosch. Native blood speckle vs ultrasound contrast agent for particle image velocimetry with ultrafast ultrasound - in vitro experiments. In *International Ultrasonics Symposium*. IEEE, 2016.

[Wer11] D. Werner. *Funktionalanalysis*. Springer-Lehrbuch, 2011.

[Whi09] F. M. White. *Fluid Machanics*. McGraw-Hill, New York, 2009.

[Wom55] J. R. Womersley. Method for the calculation of velocity, rate of flow and viscous drag in arteries when the pressure gradient is known. *J. Physiol.*, 127:553–563, 1955.

[YPO03] P.-T. Yap, R. Paramesran, and S.-H. Ong. Image Analysis by Krawtchouk Moments. *IEEE Transactions on Image Processing*, 12(11):1367–1377, Nov 2003.

[YZ11] J. Yang and Y. Zhang. Alternating direction algorithms for l1-problems in compressive sensing. *SIAM Journal on Scientific Computing*, 33(1), 2011.